

THESIS FOR THE DEGREE OF DOCTOR OF PHILOSOPHY

**Effect of Microstructure on
Mechanical Properties of High
Strength Steel Weld Metals**

Enda Keehan

Department of Experimental Physics

**CHALMERS UNIVERSITY OF TECHNOLOGY
AND
GÖTEBORG UNIVERSITY**

Göteborg, Sweden, 2004

Effect of Microstructure on Mechanical Properties of High Strength Steel Weld Metals

Enda Keehan

ISBN 91 - 7291 - 523 - 4

Doktorsavhandling vid Chalmers tekniska högskola

Ny serie nr 2205

ISSN 0346-718X

© Enda Keehan, 2004.

Department of Experimental Physics
Chalmers University of Technology
SE-412 96 Göteborg
Sweden
Telephone + 46 (0)31-772 1000

Cover: FEG-SEM micrograph of coalesced bainite

Printed and bound by Chalmers Reproservice
Göteborg, Sweden 2004

Effect of Microstructure on Mechanical Properties of High Strength Steel Weld Metals

Enda Keehan

Department of Experimental Physics
Chalmers University of Technology

Abstract

The effects of variations in alloying content on the microstructure and mechanical properties of high strength steel weld metals have been studied. Based on neural network modelling, weld metals were produced using shielded metal arc welding with nickel at 7 or 9 wt. %, manganese at 2 or 0.5 wt. % while carbon was varied between 0.03 and 0.11 wt. %. From mechanical testing, it was confirmed that a large gain in impact toughness could be achieved by reducing the manganese content. Carbon additions were found to increase strength with only a minor loss to impact toughness as predicted by the modelling. The highest yield strength (912 MPa) in combination with good impact toughness (over 60 J at $-100\text{ }^{\circ}\text{C}$) was achieved with an alloying content of 7 wt. % nickel, 0.5 wt. % manganese and 0.11 wt. % carbon.

Based on thermodynamic calculations and observed segregation behaviour it was concluded that the weld metals solidify as austenite. The microstructure was characterised using optical, transmission electron and high resolution scanning electron microscopy. At interdendritic regions mainly martensite was found. In dendrite core regions of the low carbon weld metals a mixture of upper bainite, lower bainite and a novel constituent — coalesced bainite — formed. Coalesced bainite was characterised by large bainitic ferrite grains with cementite precipitates and is believed to form when the bainite and martensite start temperatures are close to each other. Carbon additions were found to promote a more martensitic microstructure throughout the dendrites.

Mechanical properties could be rationalised in terms of microstructural constituents and a constitutional diagram was constructed summarising microstructure as a function of manganese and nickel contents.

Keywords: Strength, Impact Toughness, Neural Network Modelling, Microstructure, Martensite, Bainite, Manganese, Nickel, Carbon, Dilatometry, FEGSEM, TEM

Preface

This thesis is based on work carried out at Microscopy and Microanalysis, Department of Experimental Physics, Chalmers University of Technology, during the period 2000–2004 under the supervision of Prof. Hans Olof Andrén and with Dr. Leif Karlsson of ESAB AB as assistant supervisor. All work was carried out in co-operation with ESAB AB, Sweden and University of Cambridge, England.

The following nine papers are included in this thesis:

- I** Strong and tough steel welds
M. Muruganath, H.K.D.H. Bhadeshia, E. Keehan, H.-O. Andrén, L. Karlsson
Proc. 6th Inter. Seminar, “Numerical Analysis of Weldability”, Graz, Austria,
Oct. 1-3, 2001, Maney for The Institute of Materials, Minerals and Mining.
- II** Microstructural and mechanical effects of nickel and manganese on high
strength steel weld metals
E. Keehan, H. O. Andrén, L. Karlsson, M. Muruganath, H. K. D. H.
Bhadeshia
6th Int. Conference on Trends in Welding Research, Pine Mountain, Georgia,
USA, April 15-19, 2002, ASM International.
- III** Microstructure characterisation of a high strength steel weld metal containing
the novel constituent coalesced bainite
E. Keehan, H. K. D. H. Bhadeshia, H.-O. Andrén, L. Karlsson, L.-E. Svensson
In manuscript.
- IV** Influence of C, Mn and Ni contents on microstructure and properties of strong
steel weld metals — Part I. Effect of nickel content
E. Keehan, L. Karlsson, H.-O. Andrén
In manuscript.
- V** Influence of C, Mn and Ni contents on microstructure and properties of strong
steel weld metals — Part II. Impact toughness gain from manganese reductions
E. Keehan, L. Karlsson, H.-O. Andrén, H. K. D. H. Bhadeshia
In manuscript.
- VI** Influence of C, Mn and Ni contents on microstructure and properties of strong
steel weld metals — Part III. Increased strength from carbon additions
E. Keehan, L. Karlsson, H.-O. Andrén, H. K. D. H. Bhadeshia
In manuscript.

- VII** New developments with C-Mn-Ni high strength steel weld metals — Part A. Microstructure
E. Keehan, M. Muruganath, L. Karlsson, H.-O. Andrén, H. K. D. H. Bhadeshia
In Manuscript.
- VIII** New developments with C-Mn-Ni high strength steel weld metals — Part B. Mechanical Properties
E. Keehan, L. Karlsson, H.-O. Andrén, L.-E. Svensson
In Manuscript.
- IX** Development of High Strength Steel Weld Metals — Potential of novel high-Ni compositions
L. Karlsson, E. Keehan, H.-O. Andrén, H. K. D. H. Bhadeshia
Proceedings of Eurojoin 5, Vienna, 13-14 May, 2004.

Specification of my contributions to the included papers:

I have benefited by collaborating with several co-authors. Most microscopy and some mechanical testing within the papers has been carried out by me. All neural network simulations and X-ray diffraction experiments have been made by M. Muruganath, University of Cambridge, U.K. Thermo-Calc simulations were carried out at the Swedish Institute for Metals Research.

- I I carried out limited experimental work and helped write the paper. (This paper is included in the thesis primarily to offer the reader a greater understanding of the background to my work.)
- II I carried out most experimental work and wrote the paper.
- III I carried out all experimental work and wrote the paper.
- IV I carried out most experimental work and wrote the paper.
- V I carried out most experimental work and wrote the paper.
- VI I carried out most experimental work and wrote the paper.
- VII M. Muruganath carried out the neural network modelling. I carried out most experimental work and wrote the paper.
- VIII I carried out most experimental work and wrote the paper.
- IX I carried out microscopy and helped write the paper.

The following papers were also published during the period, but are omitted in this thesis due to overlap or because the subject is outside the scope of this thesis:

- (10) High Strength Steel Weld Metals - Developments with Ni and Mn
E. Keehan, L. Karlsson, M. Muruganath, H. O. Andrén, H. K. D. H. Bhadeshia
7th Int. Welding Symposium, pp. 797-802, Kobe, Japan, Nov. 20-22, 2001, Japan Welding Society.
- (11) Approaches to the development of high strength weld metals
D. J. Widgery, L. Karlsson, M. Muruganath, E. Keehan
2nd International Symposium on High Strength Steel, 22-23 April 2002, Verdal, Norway.
- (12) High strength steel weld metals – potential of novel high-nickel composition
L. Karlsson, E. Keehan, H.-O. Andrén, D. Widgery
12th International Symposium “Metallography 2004”, Slovakia, 28-30 April 2004
- (13) The effect of long post weld heat treatments on 2.25Cr1Mo weld metal micro-structure and properties
E-L Bergquist, L. Karlsson, M. Thuvander, E. Keehan
IIW International Congress on welding and Allied Processes - Cairo 2004, Nov. 29 - Dec. 1, 2004, Cairo, Egypt

Göteborg, November 2004

A handwritten signature in black ink that reads "Enda Keehan". The signature is written in a cursive style and is underlined with a single horizontal line.

Enda Keehan

Some wise words by fellow Irishmen

“Ever tried. Ever failed. No matter. Try again. Fail again. Fail better.”

**Samuel Beckett
(Worstward Ho)**

**“A man of genius makes no mistakes;
his errors are volitional and are the portals of discovery.”**

**James Joyce
(Ulysses)**

“As we flounder around, looking for the true measure of ourselves, we become increasingly disorientated. The trick is to stop paddling. What matters is the journey and not the destination.”

**Brian Little
(Turn Left at Greenland)**

Contents

Abstract	III
Preface	V
1. Introduction.....	1
1.1 General.....	1
1.2 Challenges.....	2
1.2.1 Strength versus toughness.....	2
1.2.2. Ductility.....	2
1.2.3. Influence of welding procedure.....	3
1.2.4. Hydrogen induced cold cracking	3
1.3 Scope of This Work.....	3
2. Welds of High Strength and Toughness.....	5
2.1 Shielded Metal Arc Welding.....	5
2.2 The effect of Welding Parameters.....	6
2.2.1 Preheat / Interpass temperature.....	6
2.2.2 Electrode diameter.....	7
2.2.3 Energy / Heat input.....	8
3. Microstructure and Alloying Additions.....	9
3.1 Microstructure.....	9
3.1.1 General.....	9
3.1.2 Solidification and the decomposition of δ -ferrite.....	11
3.1.3 The decomposition of austenite.....	11
3.1.4 Ferrite.....	12
3.1.5 Bainite.....	13
3.1.6 Martensite.....	16
3.2 Effects of Tempering.....	18
3.2.1 Tempering of Martensite.....	18
3.2.2 Tempering of Bainite.....	18
3.3 Steel Weld Metal Composition.....	20
3.3.1 Carbon.....	21
3.3.2 Manganese and Nickel.....	21
3.3.3 Chromium and Molybdenum.....	21
3.3.4 Silicon.....	22

	3.3.5 Titanium, Niobium and Vanadium.....	22
	3.3.6 Oxygen, Nitrogen and Hydrogen.....	22
4.	Modelling.....	25
	4.1 Neural Network Modelling.....	24
	4.1.1 Introduction.....	25
	4.1.2 Neural Networks Modelling.....	25
	4.1.3 Overfitting and Error Estimation.....	26
	4.1.4 Neural Network Predictions.....	27
	4.1 Thermodynamic Modelling.....	30
	4.1.1 Solidification Simulation.....	30
5.	Experimental Methods.....	31
	5.1 Production of Experimental Weld Metals.....	31
	5.1.1 The welded joint.....	31
	5.1.2 Compositions and welding parameters.....	32
	5.2 Mechanical Investigations.....	32
	5.2.1 Tensile testing.....	32
	5.2.2 Charpy impact testing.....	33
	5.2.3 Hardness testing.....	33
	5.3 Microstructural Characterisation Techniques.....	33
	5.3.1 Light optical microscopy.....	33
	5.3.2 Scanning electron microscopy.....	33
	5.3.3 Secondary ion mass spectroscopy.....	38
	5.3.4 Transmission electron microscopy.....	39
	5.3.5 Energy dispersive X - ray spectrometry.....	42
	5.3.6 Atom probe field ion microscopy.....	42
	5.3.7 X - Ray diffraction.....	44
	5.3.8 Dilatometry.....	44
	5.4 Specimen Preparation.....	46
	5.4.1 LOM, SEM, SIMS and X - Ray diffraction.....	46
	5.4.2 TEM.....	46
	5.4.3 APFIM.....	46
	5.4.4 Dilatometry.....	48
6.	Results and Outlook.....	49
	6.1 Summary of appended papers.....	49
	6.2 Concluding Remarks.....	51
	6.2 Outlook.....	51

7.	Acknowledgements.....	53
8.	References.....	55
9.	Appendix: The Papers.....	59

1. Introduction

1.1 General

Steel is arguably the world's most "advanced" material. It is a very versatile material with a wide range of attractive properties which can be produced at a very competitive production cost. It has a diverse range of applications, and is second only to concrete in its annual production tonnage. Steel is not a new invention which leads to a common misperception that "everything is known about steel" amongst those outside its field. On the contrary, research within this field is probably the most challenging of all the material sciences. It is grounded on decades of research and much fundamental theory arises from the study of steel. Steel is generally defined as a ferrous alloy containing less than 2.0 wt. % C [1]. The complexity of steel arises with the introduction of further alloying elements into the iron – carbon alloy system. The optimization of alloying content in the iron – carbon alloy system, combined with different mechanical and heat treatments lead to immense opportunities for parameter variations and these are continuously being developed.

Through the last few decades a category of steels known as high strength steels have undergone constant research. As a direct result, steels with yield strengths greater than 1100 MPa combined with good toughness at low temperatures are available such as SSAB's Weldox 1100 containing 0.2 C, 1.4 Mn, 3 Ni and minor additions of Cr, Mo, Si, Cu, V, Nb, Ti, Al and B. Today, as new and greater challenges are presented to designers and engineers, these steels are increasingly employed in a diverse range of applications such as bridges, pipelines, submarines and cranes. Constructions with lower structural thickness and weight, with the same load bearing capabilities are often possible with the employment of such steels.

In many of these applications it is essential to form strong joints that allow transfer of load between the different steel components. Generally, welding is the preferred joining method since it forms a continuous joint, it alleviates corrosion problems often associated with fasteners and it offers greater beauty to the application. In many circumstances, it is a structural requirement that the weld metal has over-matching strength in comparison to the steel in order to avoid design limitations. These requirements are possible to achieve under well controlled conditions using for example gas tungsten arc welding (GTAW). However as strength levels increase it becomes more difficult to fulfil impact toughness requirements with flexible and productive welding methods such as shielded metal arc welding (SMAW), flux cored arc welding (FCAW), or submerged arc welding (SAW) [2–3]. This project encompasses the SMAW technique with a view to increasing impact toughness of steel weld metals while keeping yield strength greater than 690 MPa (100 ksi or 10^5 lb/in²).

The ultimate goal of this project from an industrial point of view was to produce weld metals with yield strengths above 690 MPa that possess good impact toughness, are tolerant to variations in welding procedure and that have good resistance to hydrogen cracking. Some challenges that were faced will now be briefly discussed.

1.2 Challenges

There are at least four fundamental weld metal problems that every development metallurgist must address when developing high strength steel weld metals: 1. The problem of maintaining strength while increasing impact toughness; 2. Maintaining ductility within the weld metal; 3. Minimising the influence of welding procedure and 4. Avoiding hydrogen cold cracking.

1.2.1 Strength versus toughness

Strength is of little use without toughness and there is usually a trade off between the two. Toughness within the field of welding is generally expressed as impact toughness since in the majority of circumstances it is measured using a Charpy impact notch test. Any increase in strength is usually linked together with a decrease in toughness unless steps are taken to prevent it such as the refinement of the microstructure. Toughness depends mainly on composition and microstructure, for example carbon content, grain size and inclusion content. These issues are addressed in greater detail within Chapter 3.

To briefly look at the applied field, certain strength and toughness limits are usually kept in mind. These are then tested in either quality or safety tests before use. Some typical impact toughness requirements in use today for high strength applications are 47 J at $-20\text{ }^{\circ}\text{C}$ (for shipbuilding) or 40 J at $-40\text{ }^{\circ}\text{C}$ (for offshore constructions). Temperature requirements are normally set at least $30\text{ }^{\circ}\text{C}$ below the expected service temperature in many applications [4].

1.2.2. Ductility

The issue of ductility must also be addressed and it is inter-linked to the previous challenge. Ductility is a measure of the degree of plastic deformation that the weld metal can sustain before fracture. It is important for a designer to know how much plastic deformation will be experienced before fracture in order to avoid disastrous consequences in certain applications. It may be measured by percentage elongation or area reduction of tensile specimens. In the welding field, it is also taken into account taking the ratio of (Yield Strength) / (Tensile strength). The commonly required maximum value of this ratio is either 0.85 or 0.9.

1.2.3. Influence of welding procedure

Perhaps the most common challenge faced with fusion welding, e.g. the SMAW technique used here, is to minimise the influence of welding procedure. It is often possible to produce a weld metal with given desired properties under well controlled conditions in a research laboratory or factory. However, in many circumstances on the applied field, e.g. an oil rig on the North Sea, it may not be practically possible to obtain the optimum parameters. Additionally since the SMAW method is so versatile, it is the most chosen method to work with in the most awkward situations. Bearing this in mind it is understandable that the influence of welding parameters such as preheat temperature, interpass temperature, etc., should be minimised on the weld metal properties.

1.2.4. Hydrogen induced cold cracking

The topic of hydrogen cracking must also be kept in mind when designing new electrodes and steps should be taken to minimise its risk. Hydrogen cracking generally takes place below 200 °C and the cracks may form up to several days after welding. Mostly, the cracks appear in the heat affected zone (HAZ), where there is martensite, accumulation of hydrogen and high stresses. However, for high strength steel weld metals, the cracks often form in the weld metal instead. They are generally transversal to the welding direction and frequently occur between 5 and 15 mm below the surface of multilayer welds. In this area, both hydrogen concentration and resultant stresses are at their maximum.

The detailed mechanism of hydrogen cracking is not fully understood. It is dependent on three conditions in order to occur: 1. The presence of hydrogen; 2. High residual stresses; and 3. A susceptible microstructure like martensite that has a low ductility [4–5]. Hydrogen cracking is avoided in practice by using low hydrogen consumables and a controlled welding procedure often involving an elevated working temperature.

Detailed investigations into the microstructural factors affecting hydrogen induced cold cracking in high strength steel weld metals have been carried out and are presented in [6]. Within this work, it was suggested that increasing the number of interfaces in the microstructure could improve resistance by allowing the hydrogen to diffuse more uniformly within the weld metal and secondly that the presence of interfaces increased resistance to crack propagation. So far, the topic of hydrogen cracking has been outside the scope of this work but nevertheless it has been kept in mind.

1.3 Scope of This Work

In the course of this work, an attempt has been made to understand the changes in mechanical and microstructural behaviour of experimental steel weld metals as a result of variations in composition. These experimental steel weld metals are aimed at high strength applications using the SMAW technique. The weld metals examined have sim-

ilar compositions with the exceptions of nickel, manganese and carbon. The effect of these elements was examined by studying two nickel contents at 7 and 9 wt. %, two manganese contents at 0.5 or 2.0 wt. % and varying carbon content from 0.03 to 0.11 wt. %. A limited study was also done on a conventional high strength steel weld metal with 3 Ni and 2 Mn.

The composition of the new experimental weld metals have arisen out of neural network modelling carried out at the University of Cambridge. The modelling suggested that the impact strength could be increased with little loss of yield strength by reducing the manganese content at these nickel levels. Once optimum levels of manganese and nickel were reached it was predicted that the strength could be increased at moderate expense to toughness with carbon additions.

The weld metals were first tested mechanically using tensile testing, Charpy impact testing and hardness testing. Microstructural investigations were carried out using different characterisation techniques ranging from low resolution methods such as Light Optical Microscopy (LOM) to high resolution methods such as Atom Probe Field Ion Microscopy (APFIM).

Through this work an understanding was gained on how manganese, nickel and carbon affect the weld metal microstructure. Finally, it was attempted to make correlations between the microstructure and mechanical properties.

2. Weld Metal Deposition

2.1 Shielded Metal Arc Welding

Shielded Metal Arc Welding (SMAW) was used to produce all experimental weld metals analysed in this work. SMAW is also called Manual Metal Arc (MMA) welding since welding is normally carried out by a welder manually guiding a stick electrode. The set up principles of SMAW welding are shown schematically in Figure 2.1. At first glance, a normal stick electrode basically consist of a metallic wire that is surrounded by a coating, however it is much more complex. Within the electrode, there is both the filler material for the joint and intricate compounds required to control the arc, create a protective slag and generate a protective gas shroud that shields the weld pool from the atmosphere. There are four main types of coating; acidic, cellulosic, rutile and basic. These contain different quantities of minerals such as Quartz, Rutile, Flourospar, Carbonates, Ferro-alloys and Cellulose along with other organic compounds. The choice and quantity of these are determined by the required arc characteristics and the desired

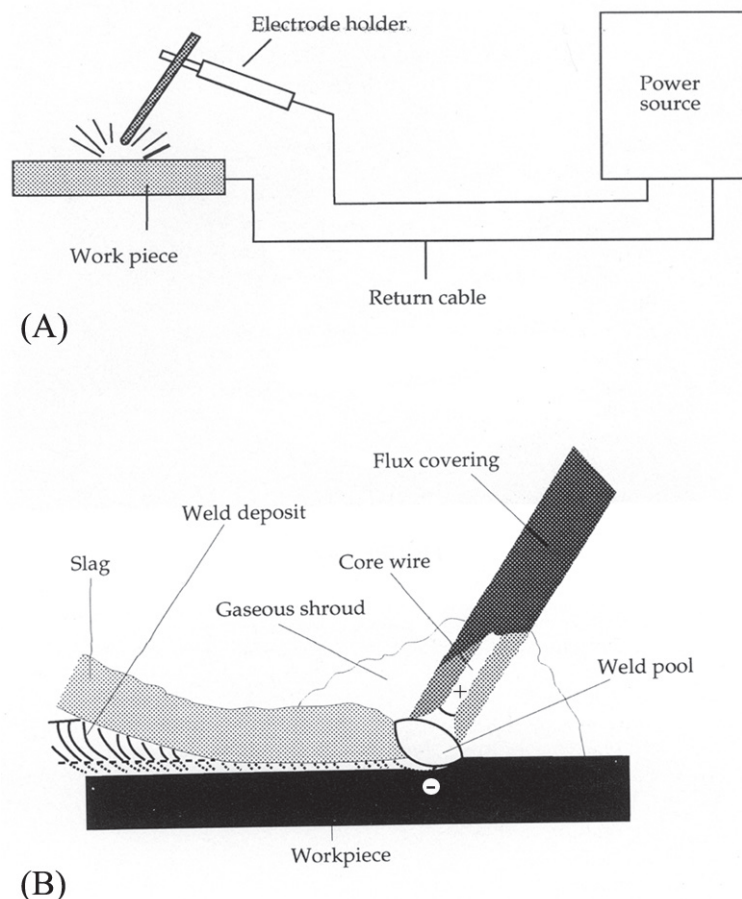


Figure 2.1. (A), showing the basic set up principles of the SMAW process. (B), showing the different components of a covered electrode and the associated weld when an arc is formed. [Ref. 7, with some minor modifications]

weld geometry to be produced. During welding the flux covering melts and in the process generates gases that help maintain a continuous flow of metal droplets from the core wire to the weld pool and also shields them from the atmosphere. It forms a viscous slag that acts as a protective layer between the molten weld metal and the atmosphere. Additionally, it shapes and holds the molten weld metal in place. The tip of the electrode is heated by resistance heating from the current passing through the metal rod which also generates the formation of an electric arc – a high current and low voltage discharge [4–5]. At this stage it is now established that there is a whole science involved in the art of welding. A closer look will now be taken on the adjustment of the weld parameters and how they affect the mechanical properties.

2.2 The effect of Welding Parameters

In SMAW it is inevitable that welding conditions vary slightly during and between each run. Within this section the options and effects of changing welding parameters are briefly discussed.

2.2.1 Preheat / interpass temperature

The interpass temperature — the temperature of the work piece before each weld run is deposited is equally important as the preheat temperature — the temperature which the work piece is first heated to. Both have a very large effect on the weld cooling rate. A minimum and / or a maximum interpass temperature may be specified and it is usually not less than the preheat temperature. A preheat temperature is sometimes required to avoid hydrogen cracking and detailed investigations to determine a suitable temperature, which is outside the scope of this work, are presented elsewhere [8]. The preheat temperature basically reduces the cooling rate and as a result minimises the hardening close to the fusion zone. In practical circumstances it may be difficult to accurately control interpass temperature and lower interpass temperatures may be encountered than what is specified. It is therefore necessary for a developer to investigate how the weld metal behaves at lower interpass temperatures once good properties have been established at desired interpass temperatures.

A specific maximum interpass temperature in welding procedure is sometimes required e.g., in order to avoid hot cracking. In this case using a higher interpass temperature will increase the time spent in the critical temperature range [9–10]. This is also an issue with high strength steel weld metals but using a high interpass temperature normally plays a more important role. Longer cooling times allows hydrogen diffusion from the weld and is a major factor when avoiding hydrogen cracking [11].

As interpass temperature is increased, the main microstructural effect is that the amount of columnar structure within a reheated weld bead is reduced and an increase in the

amount of re-austenitised and tempered areas is seen especially within the central beads of a welded joint. Little effects are seen on the cross sectional area of each weld bead deposited with increase in interpass temperature but the proportion of recrystallised area increases [12]. By eliminating the columnar microstructure, hardness becomes more uniform and is reduced. There is also a reduction in strength by increasing interpass temperature however toughness at low temperatures increases.

To conclude, control of welding parameters such as interpass temperature is important. Recent work by Lord [13] analysed the variation of mechanical properties of high strength weld metals and concluded that variations in yield strength were not alone due to compositional variations, but also to process parameters such as the weld metal interpass temperature.

2.2.2 Electrode diameter

Increasing the diameter of the electrode increases the heat input and also promotes longer weld cooling times, e.g. from 800–500 °C [12]. Additionally fewer weld layers are needed to fill the welded joint, see Figure 2.2. Increasing the electrode size increases the amount of columnar region in the weld metal. The width of the columns also increases with increase of diameter. Hardness depends on the amount of columnar structure present within the weld metal. More variations are usually seen with a larger diameter size because there is more inhomogeneity within the weld metal joint.

Increasing the electrode diameter slows weld cooling and promotes strength since it increases the proportion of the stronger as deposited microstructure. Increasing the size of the electrode decreases impact toughness at low temperatures. The negative effects that larger electrode diameter has on toughness is mainly due to the greater amount of as-deposited weld metal remaining within the weld joint.

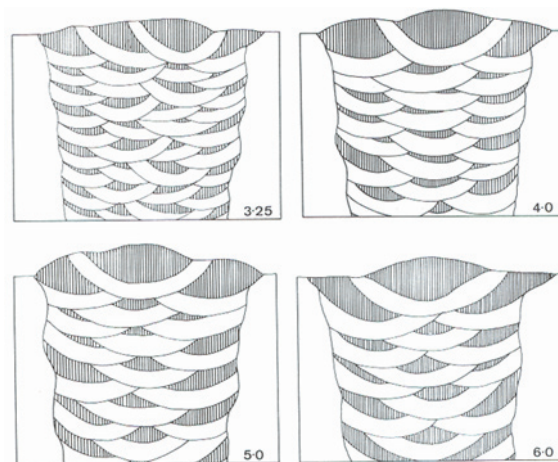


Figure 2.2 Effect of electrode size on amount of re-austenitised and tempered weld metal in multipass welding, cross sections as a function of weld diameter, white areas represent re-austenitised and tempered weld metal [12].

2.2.3 Energy / Heat Input

The energy input controls the heat generated by welding and is controlled by current, voltage, and the welding speed. In this work it was calculated using the equation [14]:

$$E = (U \times I \times 60) / (v \times 1000)$$

where E = energy input (kJ / mm)
U = voltage (V)
I = current (A)
v = speed (mm / min.)

Because of energy losses primarily due to radiation but also due to heating of the shielding gas, the value of energy input is usually factorised to account for the arc efficiency. When this is done a value is calculated for the “heat input” [11]. Since the factorisation varies between different welding conditions (typically between 0.8 and 0.95 of the energy input) it was decided to work in terms of energy input and avoid using the term heat input.

Increasing the energy input increases the area of the weld bead. Depending on joint geometry, at higher inputs fewer runs per layer are needed. Within the weld bead itself it increases the size of the different regions. In a multi-run weld with high energy input, it is possible to remove most of the columnar structure in the joint centre. Mechanically, both the average hardness and strength drop with increase in energy input [12].

3 Microstructure and Alloying Additions

3.1 Microstructure

3.1.1 General

High strength steel weld metals with yield strengths up to 700 MPa and higher are available. Microstructures suitable to resist stresses of such magnitude, are usually composed of, or a combination of, martensite, bainite, retained austenite and acicular ferrite. Prior to these final constituents, the weld metal will have undergone complex changes and transformations as it cools from its liquid form when deposited. This may be clearly seen in the basic phase diagram of steel showing the iron - carbon system as presented in Figure 3.1.

However, one must bear in mind, that there are a few characteristic differences between the microstructure of weld metals and those of wrought steels. Once wrought steel is formed, various types of heat treatment may be performed in order to adjust both the microstructure and the mechanical properties. However, with weld metals this is not normally the case, and in many circumstances it is not possible. Weld metals are

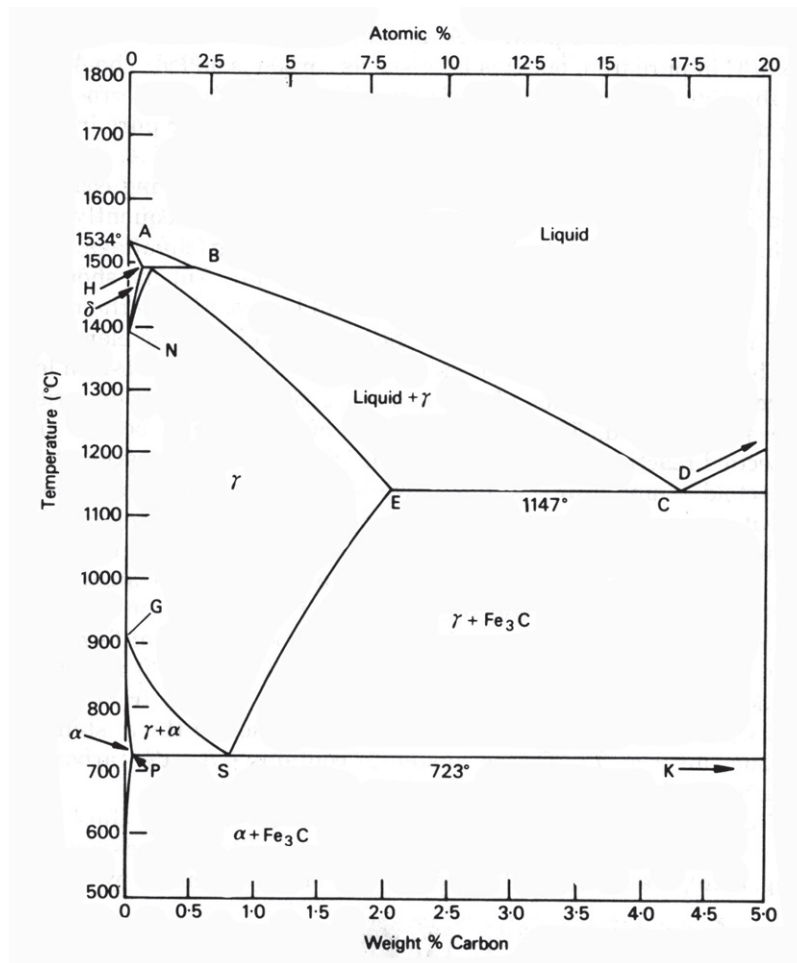


Figure 3.1 The iron-carbon phase diagram [22]

cast materials and their cooling conditions are very different in comparison to that of a steel that has undergone forging or rolling. Other characteristic differences between the two is the frequent presence of non-metallic inclusions within weld metals and also segregation. The occurrence of interdendritic segregation must always be kept in mind when investigating the weld metal microstructure. Basically there is a difference in composition between the core and the other portions of the dendrite that formed during solidification. As alloying is increased it plays a more important role in determining the microstructural transformations that take place and it may lead to different phases in the dendrite-core and in interdendritic regions. Microsegregation allows the formation of microstructures that are hard to produce in any other metallurgical process. This can be beneficial when it is properly controlled but can create a lot of difficulties with for example cracking when not. When weld metals are deposited in multi runs or if they are heat treated, part of the previous bead is reheated to a high temperature and the bead is no longer in the “as deposited” condition. Microsegregation can be partially removed, however, a long annealing time is needed to remove it completely [15].

A brief overview of some phase transformation mechanisms that occur in high strength steel weld metals will now be given; comprehensive treatments of the physical metallurgy may be found in [1, 4–5, 11, 16–18].

3.1.2 Solidification and the decomposition of δ -ferrite

When welding in particular material with similar or the same composition as the molten weld metal, epitaxial growth rather than nucleation occurs. Epitaxial growth is where the molten liquid solidifies and develops new grains directly from the solid in the underlying material. Solidification generally occurs along the maximum thermal gradient towards the weld centre resulting in a columnar solidification structure. The width of the columns are usually related to the size of the grains in the underlying bead. It is normally expected that the grains increase in size and are expected to be wider than the underlying grains. Grains separated by high angle boundaries are called the primary grains and it is usually found that there is a substructure divided by low angle grain boundaries within the primary grains. The substructure develops in different ways depending on the solute content, the thermal gradient and the solidification velocity. Four different modes are usually found; planar front, cellular, cellular dendritic and dendritic. In this particular work the mode of cellular dendritic was applicable which is a combination of cellular and the dendritic growth mechanisms. Growth occurs from the motion of an unstable solidification front and dendrites develop sometimes with a slight deviation from the maximum thermal gradient direction following the easy growth direction of $\langle 100 \rangle$.

Most steel weld metals begin their solidification with the formation of δ -ferrite and in the majority of cases it is accompanied by nucleation of austenite on the δ - δ ferrite

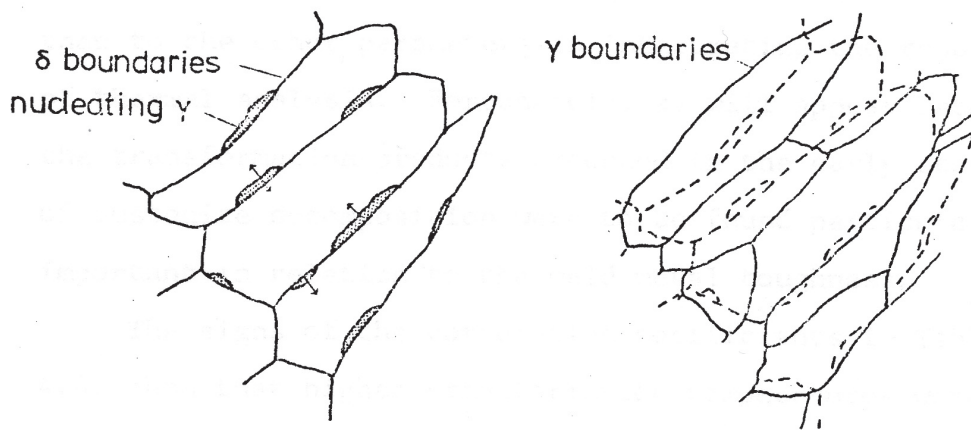


Figure 3.2 Schematic diagram showing the development of columnar austenite grains from the primary δ -ferrite solification structure. [19]

grain boundaries as shown in Figure 3.2. The δ -ferrite grains that form on solidification are reported to have an elongated or columnar structure [4, 20]. When δ -ferrite forms, two major solid phase transformations occur on cooling to room temperature. The first occurs at high temperatures with δ -ferrite (Body Centered Cubic (B.C.C)) transforming to austenite (Face Centered Cubic (F.C.C.)) approximately between 1400 and 1500 °C. The austenite is reported to grow from side to side across the δ -ferrite grains with some uncertainty about the exact mechanism as it is generally not possible to clearly see the former austenite boundaries after transformation has taken place at lower temperatures [4]. In any case, the formation of austenite happens very quickly and its grain size is a very important factor. The austenite grain size has an influence on the γ to α -ferrite transformation (next section), and on the final mechanical properties.

The formation of δ -ferrite may be prevented entirely by fast cooling, increasing carbon content or with additions of manganese or nickel [21–22]. When austenite forms directly from the molten weld metal the austenite grain size is expected to be larger than if it were formed from the decomposition of δ -ferrite. [23] Additionally, only one major solid phase transformation takes place on cooling to room temperature.

3.1.3 The decomposition of austenite

The second solid transformation, the decomposition of austenite, takes place below 800 °C and the exact temperature depends on cooling rate and alloying content, with austenite (F.C.C.) transforming to α -ferrite (B.C.C.). The decomposition of austenite is generally shown in the form of a continuous cooling transformation (CCT) diagram such as that in Figure 3.3. Understanding the reactions and factors that control these curves have been the focus of metallographic investigations for decades within steel research.

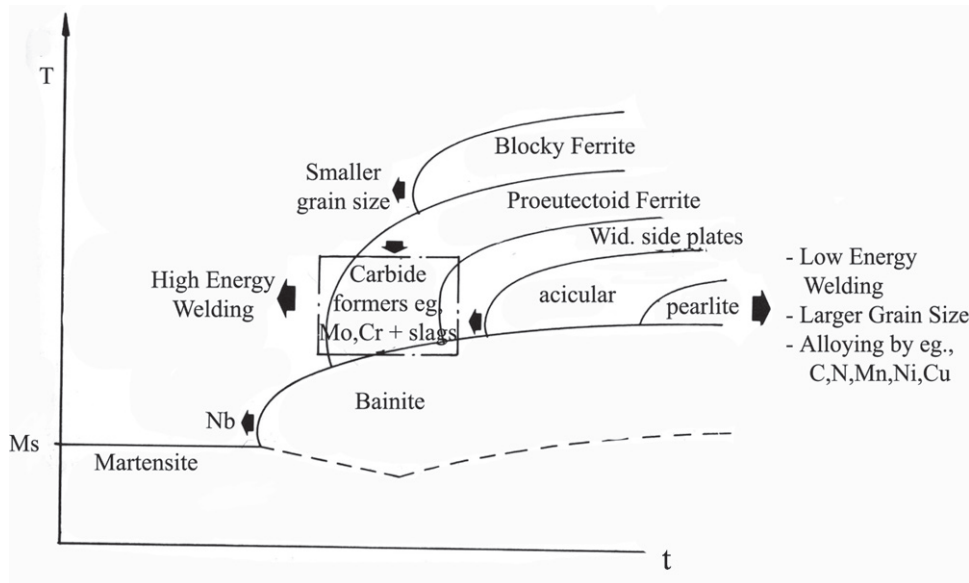


Figure 3.3 CCT diagram for steel weld metal, summarising the possible effects of microstructure and alloying on the transformation products for different weld cooling times [16].

The microstructural transformations that take place are largely dependant on both the cooling rate and the composition. In steel, it was reported that austenite transformed to ferrite on cooling between 910 and 723 °C in iron – carbon alloys [1]. At fast cooling, the transformation temperature may be depressed below the region of 690 °C with austenite transforming to upper bainite. At even higher cooling rates transformation can take place in the region of 500 °C or lower, i.e. the martensite start temperature (M_s) (that depends on alloying) [5].

The remaining part of this section will describe briefly the microstructural morphologies and the transformation mechanisms of the weld metal as it decomposes from austenite. In high strength steel weld metals, as strength levels increase above the region of 690 MPa, the microstructures are largely bainitic, martensitic and sometimes with small amounts of acicular ferrite.

3.1.4 Ferrite

There are three main ferritic constituents that form in weld metals; allotrimorphic ferrite, Widmanstätten side plates and acicular ferrite. Allotrimorphic ferrite and Widmanstätten side plates are generally not observed in high strength steel weld metals due to the high alloying content. As a result these will not be discussed further and instead focus will be placed on acicular ferrite.

Acicular ferrite is generally found to be positive for impact toughness. It is called acicular due to its needle shape in two dimensional sections. In three dimensions it is found to be in the form of lenticular plates with dimensions in the order of 5 to 10 μm

in length and around $1\mu\text{m}$ in diameter. It nucleates on inclusions inside the austenite grains. In literature it is sometimes described as an intragranularly nucleated bainite. [5] Arguments put forward to designate it as bainite were the shape change accompanying the transformation which is an invariant-plane strain with a large shear component, a similar stored energy of transformation of around 400 J/mol , no bulk partitioning of substitutional alloying element on formation, the orientation relationship between it and the parent austenite and finally “the incomplete – reaction phenomenon” where the degree of reaction tending towards zero as the transformation temperature approaches the bainite start (B_s) temperature. [5] The big difference between classical bainite and acicular ferrite is the fact that it nucleates intragranularly in the form of isolated plates radiating from a point nucleation site rather than the sheaf morphology of classical bainite which nucleates at austenite grain boundaries.

3.1.5 Bainite

Bainite was first discovered in the early 1930’s by Davenport and Bain [24] who were investigating the isothermal transformations of austenite. It was called “Bainite” by the staff at the United States Steel Corporation Laboratory after E.C. Bain who had initiated the studies. From the early days it was known that there were two types of bainite; upper bainite formed at high temperatures and lower bainite formed at low temperatures [25]. A schematic of both is shown in Figure 3.4.

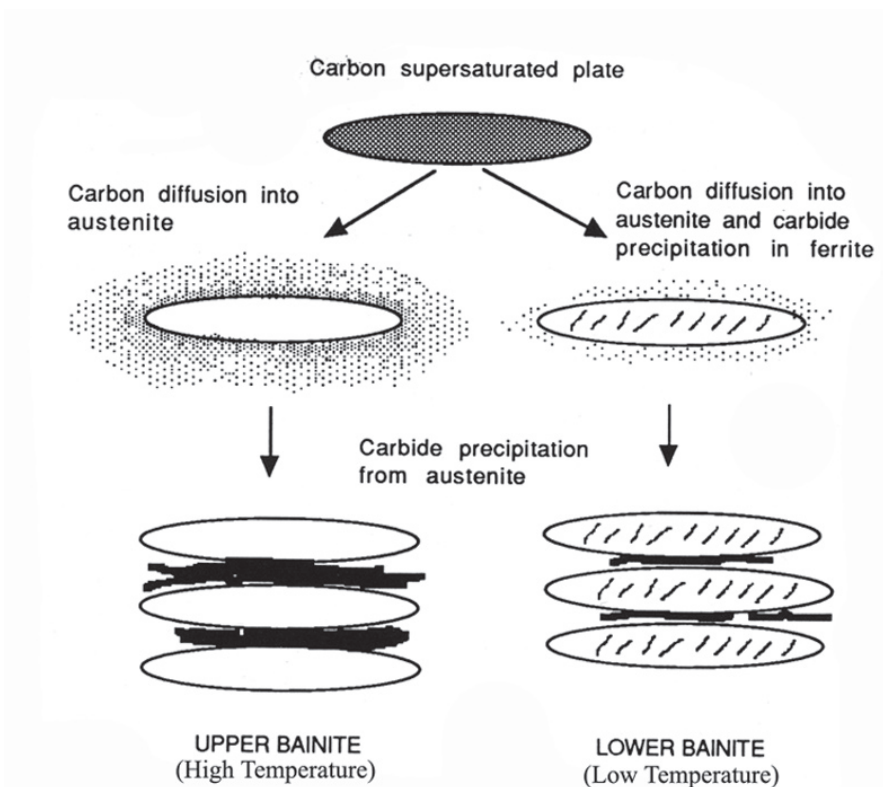


Figure 3.4 Schematic of the transition path to both upper and lower bainite [18].

At transformation temperatures in the region of, or less than 690 °C, carbon doesn't have time to diffuse into austenite as ferrite nucleates on the austenite grain boundaries [5]. To cope with this, the carbon concentrates and redistributes at the phase boundary since the solubility of carbon in bainitic ferrite is low (< 0.02 wt.% [1]). As the carbon content increases at the phase boundary it may reach a high enough concentration at which cementite is able to nucleate and grow. Depending on the level of carbon, cementite may be in the form discrete particles (at low concentrations), or as continuous layers separating the ferrite plates (at high concentrations).

Cementite or M_3C is an iron rich carbide where sometimes the iron atoms can be replaced and other elements can be taken into solution. It has an orthorhombic structure with space group Pbnm, and Fe_3C has lattice parameters $a = 0.4523$ nm, $b = 0.5088$ nm and $c = 0.6743$ nm. Figure 3.5 shows the unit cell of cementite where there are 16 atoms in total, 12 metal atoms and 4 carbon atoms. Strong carbide forming elements such as Cr, Mo, W, V and weaker elements such as Mn, Ni and Co can be found in solution in M_3C . It is formed by eg. eutectoid and bainitic decomposition of austenite or precipitation in ferrite during tempering.

As each plate of bainitic ferrite grows it changes shape and is accompanied by a large strain which can be described as an invariant – plane strain with a large shear component similar to that of martensite [1, 18, 32]. The change of shape and mechanism of growth indicate that the transformation mechanism is displacive rather than reconstructive. The

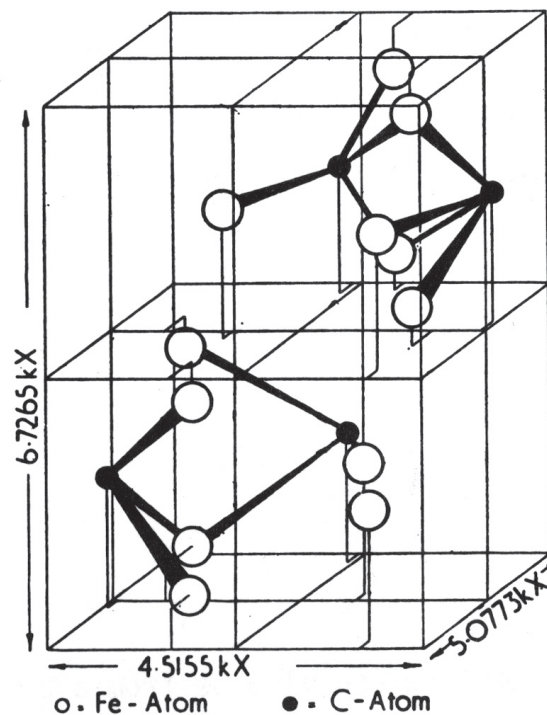


Figure 3.5 The unit cell of cementite, Fe_3C [68]. ($1kX = 1.00202 \text{ \AA}$)

two methods of atomic rearrangement, reconstructive transformation and displacive transformation are described in detail in [32]. Reconstructive transformation is the breaking of all bonds and rearranging the atoms into another alternative pattern while displacive transformation is described as homogeneously deforming the original pattern into a new crystal structure. Displacive transformation also alters the macroscopic shape unless it is constrained. During constrained rearrangement, transformation occurs by the combination of elastic and plastic strains in the surrounding matrix. The product grows in the form of thin plates, which reduces the strains. To conclude, bainite fulfils all criteria for the displacive mechanism of transformation.

Since bainitic ferrite is generated through a coordinate movement of atoms, it follows that there is an orientation relationship between bainitic ferrite and the parent austenite. The austenite-bainitic ferrite orientation relationships are described by the Niashiyama–Wasserman orientation relationship [26] for upper bainite and the Kurdjumov–Sachs orientation relationship [27] for lower bainitic – ferrite, according to the classic paper by Smith and Mehl [28]. However, later investigations revealed a scatter in the observed relationship between the exact NW and KS orientations [29]. From these investigations it was reported that the close packed plane of bainitic ferrite is found to be parallel or nearly parallel to the close packed plane of austenite. It was also found that the close packed planes of bainitic ferrite were parallel or nearly parallel to the close packed direction in austenite. The orientation relationships reported were: -

$$\text{NW: } \{111\}_{\gamma} // \{011\}_{\alpha}$$

$$\langle \bar{1}01 \rangle_{\gamma} // \langle \bar{1}\bar{1}1 \rangle_{\alpha}$$

$$\text{KS: } \{111\}_{\gamma} // \{011\}_{\alpha}$$

$$\langle \bar{1}01 \rangle_{\gamma} \text{ about } 5^{\circ} \text{ from } \langle \bar{1}\bar{1}1 \rangle_{\alpha} \text{ towards } \langle 1\bar{1}1 \rangle_{\alpha}$$

$$\langle 11\bar{2} \rangle_{\gamma} // \langle 0\bar{1}1 \rangle_{\alpha}$$

The cementite particles that form during the upper bainite transformation have the Pitsch orientation relationship with the parent austenite.

$$[001]_{\text{Fe}_3\text{C}} // [\bar{2}25]_{\gamma}$$

$$[100]_{\text{Fe}_3\text{C}} // [5\bar{5}4]_{\gamma}$$

$$[010]_{\text{Fe}_3\text{C}} // [\bar{1}\bar{1}0]_{\gamma}$$

When there are adequate quantities of alloying elements such as Si or Al the formation of cementite may be prevented completely. When this is the case a microstructure of bainitic ferrite separated by retained austenite is obtained. Martensite may also be present in this microstructure if the austenite decomposes further at lower temperatures.

At slightly faster cooling rates than needed for an upper bainite transformation, the austenite will reach lower temperatures with transformation taking place in the region of 500 °C. When transformation occurs at these temperatures, carbon diffusion is slow within the austenite and only occurs at short ranges. As the ferrite plates grow, they prefer to remove the carbon at the interface through the repeated precipitation of cementite. In doing so any excess carbon at the interface is lost and the interface advances again.

This latter cementite formed follows the Bagaryatski orientation relationship with the ferritic plates. This relationship is also found with carbides that precipitate on the heat treatment of martensite [1]. The Bagaryatski relationship is described as: -

$$[001]_{\text{Fe}_3\text{C}} // [\bar{1}01]_{\alpha}$$

$$[100]_{\text{Fe}_3\text{C}} // [111]_{\alpha}$$

$$[010]_{\text{Fe}_3\text{C}} // [\bar{1}2\bar{1}]_{\alpha}$$

3.1.6 Martensite

At the fastest cooling rates, the austenite may reach the region of 400 °C or below depending on alloying, before transformation. Transformation at these temperatures is a diffusionless process producing lath martensite. No single atom moves more than one lattice spacing. Martensite may be considered as a supersaturated solution of carbon in α iron. It has a body centered tetragonal (B.C.T.) structure. Since the transformation is from F.C.C. to B.C.C. and is also diffusionless, the interstitial carbon atoms are limited to the one common octahedral site in both the F.C.C. and B.C.C. structures. The three possible octahedral sites are shown in Figure 3.6. The z-sites in this figure are the octahedral sites common to both structures and will therefore be occupied by carbon. As a result an expansion in the z direction is experienced. This is a unidirectional distortion and bring about the change from B.C.C. to B.C.T. The change to B.C.T. distinguishes martensite from supersaturated ferrite. In supersaturated ferrite all interstitial sites have equal probability of occupation [30]. When only substitutional solutes are present the transformed product is cubic while it is generally tetragonal if there are interstitial solutes present. It was reported that martensite in iron-nickel-carbon alloys with only ~ 0.05 % carbon is tetragonal, provided that the M_s temperature is sufficiently low to prevent autotempering during the quench [31].

As with bainite, martensite has an orientation relationship with the parent austenite. It was stated that orientation relationships between martensite and austenite varies with composition, however in all ferrous alloys a $\{111\}_\gamma$ plane is approximately parallel to the $\{011\}_{\alpha'}$ plane (where, γ denotes austenite, α' denotes martensite). Additionally, within these two close packed planes there is a possible variation in orientation of ~ 5.5 degrees from approximately Kurdjumov–Sachs relation to the Nishiyama relationship [30]. These relations are described as:

$$\langle \bar{1} 0 1 \rangle_\gamma // \langle \bar{1} 1 1 \rangle_{\alpha'} \text{ (Kurdjumov–Sachs relation)}$$

$$\langle 1 1 \bar{2} \rangle_\gamma // \langle 1 \bar{1} 0 \rangle_{\alpha'} \text{ (Nishiyama relationship)}$$

The lattice corresponding to the transition of austenite to α martensite was first pointed out by Bain who showed the tetragonal structure could be outlined within two unit cells of austenite as shown in Figure 3.7 [30]. In order to obtain the martensite cell, a contraction caused by the Bain strain of about 17 % along the $[001]_\gamma$ (martensite c-axis) and an expansion of about 12 % in the $(001)_\gamma$ is needed. The crystallography of displace transformation was clearly described by Bhadeshia in a review paper on steel phase transformations [32]. When the Bain strain (B) is in parallel with a rigid body rotation (R) as shown in Figure 3.7, the resultant lattice deformation RB is an “invariant line strain” that gives good fit along a single line common to both crystals. The shape change induced is an invariant plane strain P1 but this gives the wrong crystal structure. However when P1 is combined with a homogeneous shear (P2), the correct structure

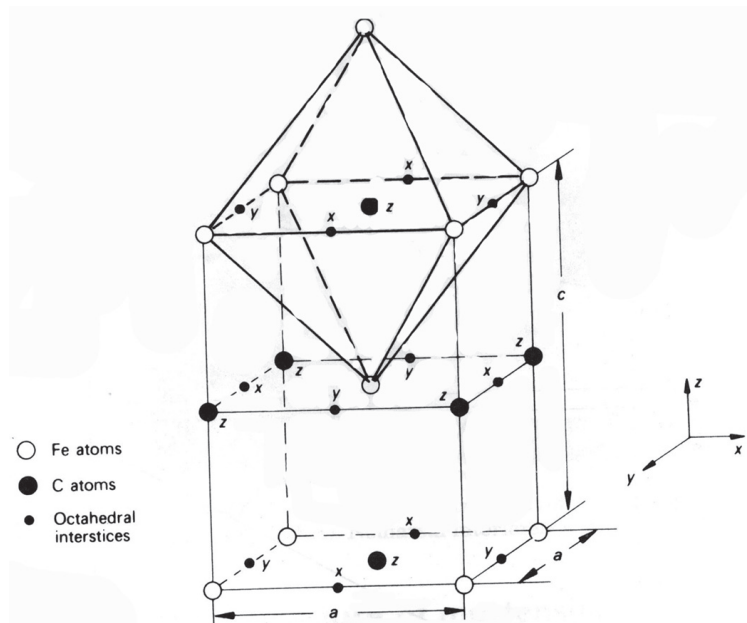


Figure 3.6 Martensite body centered tetragonal lattice showing the three sets of octahedral interstitials. The Z - set is fully occupied by carbon atoms [1].

is obtained but the wrong shape, since $P1 \times P2 = RB$. All criteria are fulfilled when the overall effect of P2 is cancelled by an inhomogeneous lattice invariant deformation that may be slip or twinning as shown in Figure 3.8

3.2 Effects of Tempering

Tempering is a term that comes originally from the heat treatment of martensite. It generally describes how both the microstructure and properties change as a result of holding a sample isothermally below the austenite formation temperature. In multi-pass welding, the microstructure is deemed to be tempered once the weld metal has been heated to temperatures below austenite formation as a result of the deposition of a weld bead(s) on top of an underlying bead(s).

3.2.1 Tempering of Martensite

In literature, it is generally agreed that there are four stages in the tempering of martensite. During the first stage which takes place at low temperatures (up to 250 °C), carbon in solid solution begins to segregate to defects and forms clusters. It then precipitates to form cementite or ϵ -carbide which has a close packed hexagonal structure. Stage 2 happens in the region (230–300 °C) where the majority of the carbon is precipitated, ϵ -carbide transforms to cementite which is more stable and any austenite retained during quenching decomposes. During Stage 3 cementite appears and this can happen between approximately 100–300 °C. Also the tetragonality in high carbon martensite disappears and the microstructure becomes ferrite not supersaturated in carbon. Tempering at even higher temperatures (300–700 °C) results in Stage 4 where the cementite particles start coarsening, they lose their crystallographic morphology and become spheroidised. Additional effects at high temperatures are the recrystallisation of ferrite plates into equiaxed grains which also promotes a reduction in the dislocation density. Alloy carbides begin to form in the range 500–600 °C and their formation depends largely on the alloying content and the presence of carbide forming elements. If they form a secondary hardening effect may be experienced where fine alloy carbides develop at the expense of cementite. [1, 18]

The observed effects of tempering martensite on mechanical properties are dependent on the carbon content within the martensite, the alloying content and the tempering temperature. For hardness the general trend is softening as the tempering temperature is raised. A reduction in yield and tensile strength is also normally observed while toughness is found to increase as tempering temperature increases. [1]

3.2.2 Tempering of Bainite

There are important differences in the tempering of bainite from that of martensite because bainite only contains a slight excess rather than a supersaturation of carbon

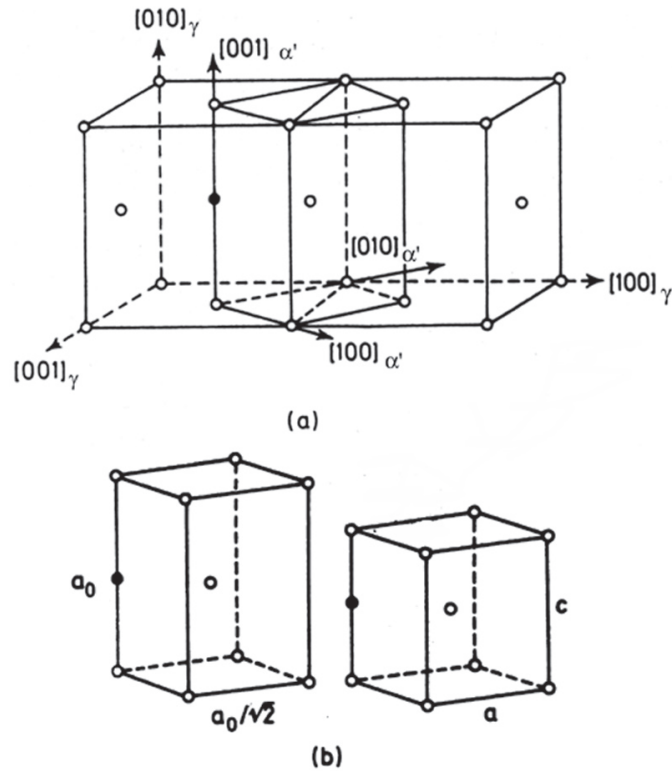


Figure 3.7 The lattice corresponding to the formation of martensite. (a) The B.C.T. cell of base edge length $a_0 / 2^{1/2}$ outlined in the austenite structure of cell size a_0 . (b) deformation (Bain strain) along the c axis carries this structure into martensite cell with parameters a, c . Open symbols represent iron atoms, filled symbols represent one possible carbon site [34].

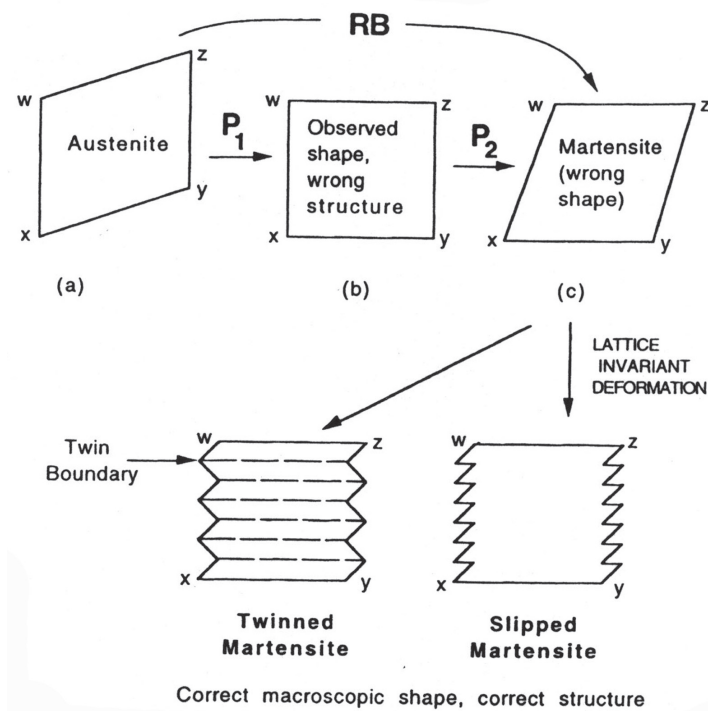


Figure 3.8 The crystallographic theory behind displacive transformation [20]. The figure is explained within the text.

in solution and it also autotempers during transformation. A lot of the carbon partitions out or precipitates during the bainite reaction. The carbon is generally located within the cementite that forms which is usually coarser than that formed from tempering martensite. Bainite is normally less sensitive to tempering in comparison to martensite.

If bainite formation takes place at high temperatures it may experience some recovery of the dislocation substructure. Normally, only minor changes in recovery, morphology or carbide precipitation occur during tempering. The largest effect of tempering is observed when the plate-like structure of ferrite changes to equiaxed ferrite. Spheroidisation and coarsening of cementite also take place with this change. Secondary hardening may also be experienced with bainite at high temperatures but it is normally much more sluggish since the cementite tends to be coarser in bainite.

Strength decreases with the tempering of bainite but the extent is not as dramatic as with martensite because there is little or no carbon in solid solution. Carbon is normally present in the form of carbide which contribute little to strength. Changes in strength may be observed as the microstructure coarsens or when recrystallisation takes place at high temperatures and equiaxed grains of ferrite replace the bainite plates. Minor changes may also occur due to the coarsening of cementite particles or the recovery of the dislocation substructure. [1, 18]

3.3 Steel Weld Metal Composition

Solid solutions are formed when alloying elements such as carbon, manganese or nickel are dissolved atom by atom either interstitially or substitutionally. When the matrix is saturated with a particular element, a separate phase can form. As a weld metal is either cooled or heated certain elements may inhibit phase transformation in the steel. For example, austenite stabilisers are nickel, cobalt, carbon, manganese and nitrogen while ferrite stabilisers are silicon, chromium, tungsten, molybdenum, vanadium and niobium. Alloying also plays a role in mechanical behaviour of the weld metal. Grain refinement is the most favoured strengthening mechanism in high strength steel weld metals as it also contributes to toughness. Precipitation strengthening is also a favoured strengthening mechanism. In order to provide some resistance to brittle cleavage fracture, alloying with some substitutional solutes helps to improve toughness. Leslie reported the following list of elements in decreasing effectiveness improve the toughness of iron; Pt, Ni, Ru, Rh, Ir and Re [33]. Of these the only one feasible is Ni. This section examines the effect of the different elements on both microstructural phases and mechanical properties.

3.3.1 Carbon

Carbon content is important to the overall strength and hardness of the weld metal. The location of carbon atoms, whether they remain in solution or if they are precipitated, determines whether the steel is martensitic or ferritic. The level of carbon is critical for optimising microstructure and mechanical properties.

Greater additions of carbon lowers the martensite transformation temperature. Increasing the amount of martensite with higher carbon in the HAZ raises the risk of hydrogen cracking and also decreases toughness. At too low carbon contents ferrite may form so carbon is made up for by increasing the alloying content [10].

The carbon content is also directly related to the risk of solidification cracking. At high carbon levels greater amounts of Mn and lower levels of S are required in order to avoid this type of cracking. The carbon and sulphur content is generally kept low in welding consumables and solidification cracking is not a major problem [10].

3.3.2 Manganese and Nickel

The alloying content of manganese and nickel are very important in the solidification process in high strength steel weld metals. Large additions of these elements can prevent the formation of δ -ferrite entirely and instead the weld metal solidifies directly to austenite as shown in Figures 3.9, 3.10 and 3.11. [21–22]

Additional effects of manganese is that it gives strengthening through solid solution hardening and grain refinement by lowering the austenite to ferrite transformation temperature. Grain refinement also leads to increased toughness. Unfortunately manganese tends to segregate which promotes variations in hardness and microstructure. It also forms inclusions that may be detrimental to the toughness. Manganese is generally limited to minimise solidification segregation [10, 34]. Manganese combines with sulphur and reduces the risk of solidification cracking [12].

Nickel improves toughness, adds a solid solution hardening effect and increases quench hardenability [34]. It is also believed to influence the stacking fault energy of ferrite in such a manner that plastic deformation is accommodated at low temperatures [4].

3.3.3 Chromium and Molybdenum

These elements are well known in the alloying of steel. Chromium stabilises ferrite but slows down transformation rate. It also increases hardness and strength and has a greater influence when manganese is at low concentrations [12]. With chromium additions, toughness falls as reported in studies of mechanical properties of high strength steel weld metals [21, 36]. It provides solid solution strengthening and promotes carbide formation. Both chromium also increases hardenability and gives both oxidation

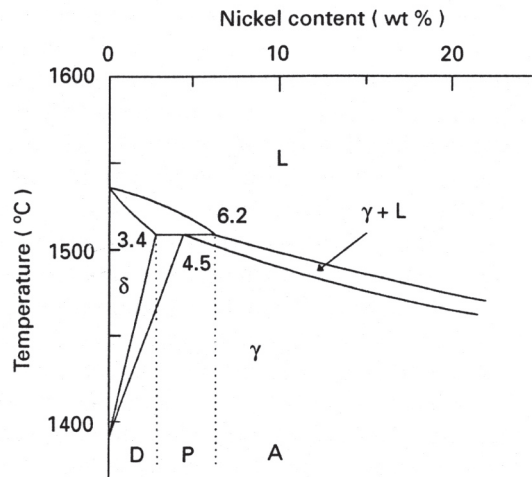


Figure 3.9 Fe-Ni equilibrium phase diagram (high temperature section). [35] (D: primary δ -ferrite solidification, P: peritectic solidification, A: primary austenite solidification).

and corrosion resistance [34]. Chromium and molybdenum increase resistance to high temperature corrosion and are well known for giving resistance against creep in heat resistant steels.

3.3.4 Silicon

Silicon contributes a large solid solution hardening factor. The addition of silicon (in high concentrations, 1.5 wt. %) is reported to eliminate poor toughness in bainitic steels [32]. Silicon has poor solubility in cementite and retards its precipitation.

3.3.5 Titanium, Niobium and Vanadium

Titanium, niobium and vanadium are microalloying elements. These elements can form precipitates in the form of carbonitrides but are in very low quantities in high strength steel weld metals. If precipitation takes place, it contributes to strength through precipitation hardening. Titanium and boron increase toughness at low temperatures [4, 34]. Titanium is also known to form oxides.

3.3.6 Oxygen, Nitrogen and Hydrogen

Oxygen, nitrogen and hydrogen are the three main absorbed gases within weld metals. Oxygen reduces both the strength and toughness. It is difficult to determine how much is in solid solution since it tends to be present in finely dispersed oxygen rich microscopic inclusions. These microscopic inclusions are an inevitable part of welding and in SMAW their size is determined by the electrode coating type and energy input. Oxides can be in the form of iron-manganese oxide in neutral and acidic weld metal with the latter containing some iron-manganese-silicate oxides while the basic type weld metals

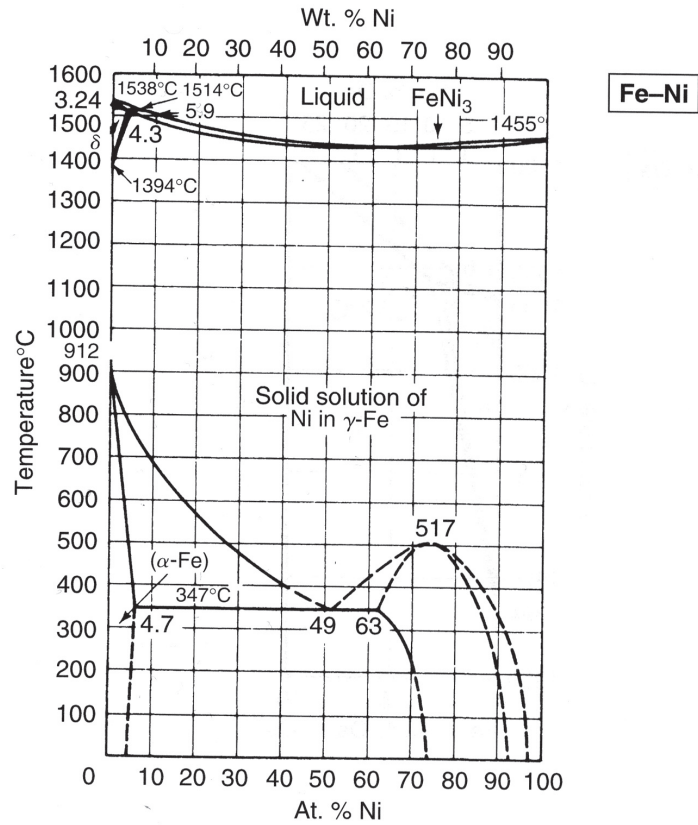


Figure 3.10 The complete Fe-Ni equilibrium phase diagram. [37]

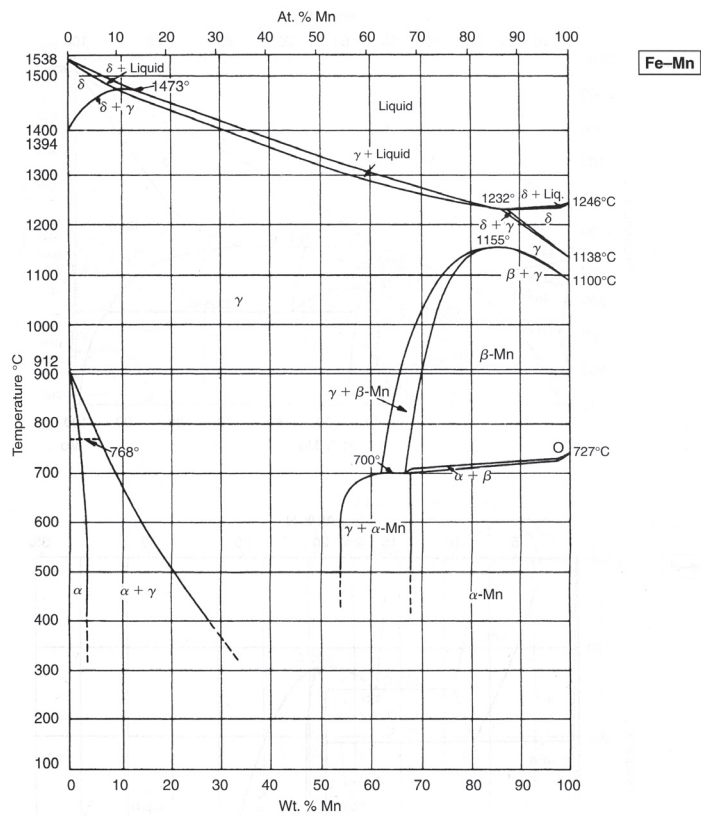


Figure 3.11 The Fe-Mn equilibrium phase diagram. [37]

almost only contain iron-manganese-silicate oxides [15]. Oxygen also combines with iron to form FeO and separates out as slag.

Nitrogen raises the strength but reduces the toughness. Nitrogen is normally present in ppm concentration but may still have a large effect on the mechanical properties. Too long an arc may lead to excess nitrogen pick up [4]. Excess nitrogen is ejected in the form of gas or may cause porosity.

Hydrogen has a high solubility in iron because of its small atomic radius and dissolves easily in the solidifying weld metal. Although it is present in solution while welding it diffuses out as the weld metal cools. When practical any remaining hydrogen can be removed by a low temperature (< 300) soaking heat treatment. Hydrogen within the weld metal reduces ductility.

4. Modelling

4.1 Neural network modelling

4.1.1 Introduction

As we have seen in Chapter 2 and 3, the design of high strength steel weld metals is very complex. There are a wide variety of parameters each having their own individual effect, or a combined effect, on the final microstructure and mechanical properties. Given that our task is a complex one, it was decided to engage neural network modelling to allow both the optimization of the welding process and to investigate the effects of a wide variety of parameters quickly and cheaply. The modelling for this project was carried out at the University of Cambridge and only a brief summary will be given here. Further details about the technique of neural network modelling may be found in [38–41].

Many scientists are acquainted with the use of creating and applying linear regression equations to experimental data. Creating a linear regression equation basically involves taking the sum of each input or operating parameter x_j and multiply it by a certain factor or weight w_j , which is determined by how much it influences the final outcome or properties. A constant θ , is then added to the sum, giving an equation that makes a estimate of the outcome of the process or property y , i.e. $\sum w_j x_j + \theta = y$. There are many examples of this type of equation in materials science. Two examples are; equations for predicting the martensite start temperature M_s and equations for predicting the bainite start temperature B_s .

Although linear regression analysis is very helpful, there is however a few difficulties associated with the method. The first problem is that the relationship must be chosen before the equation of model is applied. Secondly, the relationship is normally linear with non-linear terms added to form a pseudo-linear equation and once it is derived it is applied to the complete range of input space. This may not be reasonable as the relationships may vary across the input space. A method that avoids these difficulties is neural networks.

4.1.2 Neural Networks

Neural network modelling employs the use of non - linear regression equations in its predictions. With this method, the linear functions of the input x_j are multiplied by the weight w_j and is then operated on by a hyperbolic tangent transfer function. The equation becomes:

$$h = \tanh \left(\sum_j^N w_j^{(1)} x_j + \theta^{(1)} \right)$$

$$\text{with, } y = w^{(2)} h + \theta^{(2)} \quad \text{where, } w^{(2)} \text{ and } \theta^{(2)} \text{ are additional constants}$$

Figure 4.1 (a) Three different hyperbolic functions; the “strength” of each depends on the weights. (b) A combination of two hyperbolic tangents to produce a more complex model. [Ref. 38, with modifications]

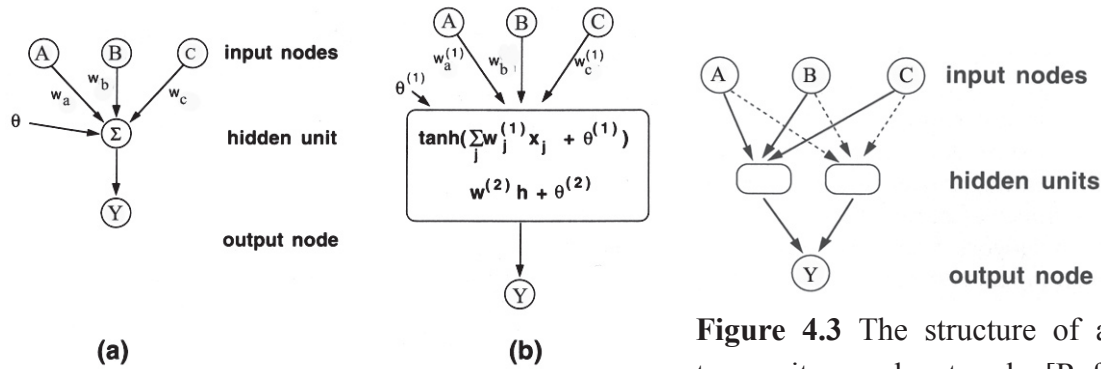
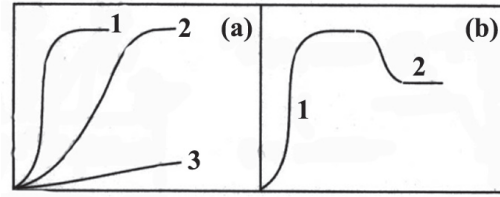


Figure 4.2 (a) A network representation of linear regression analysis (b) A non-linear network representation [Ref. 38, with minor adjustments]

Figure 4.3 The structure of a two unit neural network. [Ref. 38, with modifications]

The hyperbolic tangent function is chosen because of its flexibility across input space and it can be varied in the different regions through adjustment of the weights w_j as shown in Figure 4.1. As a result, the output y , is a non-linear function of x_j and the difficulties associated with linear regression analysis are avoided. A schematic neural network comparison of the two methods is shown in Figure 4.2.

In the majority of circumstances a one hidden-unit models may not be sufficiently flexible over the entire range of input space and in this case greater non-linearity is added by combining a number of hyperbolic tangent functions. The output function for i hidden units becomes:

$$y = \sum_i^N w_i^{(2)} h_i + \theta^{(2)} \quad \text{where, } h_i = \tanh \left(\sum_j^N w_{ij}^{(1)} x_j + \theta_i^{(1)} \right)$$

The extra flexibility added allow greater fitting to be achieved. It also allows the interaction between different inputs to be accounted for. A schematic of a two hidden-unit neural network model is shown in Figure 4.3.

4.1.3 Overfitting and Error Estimation

Since so much flexibility has been introduced to the method with the addition of extra hidden units, the problem of overfitting data may now arise. To alleviate this, the experimental data is divided into two sets — the training data and the test data. The model is

created using the training set of data. It is then tested using the unseen or test data to see that it performs well. The model may have large error if it is over-simplified in relation to the input data and it may not be able to represent the complexity of the data. Opposing this, a large error within the model may arise if the model is too complex and it is falsely modelling the noise within the experimental data. Training the model achieves the optimum non-linear relationship between the input and the output. It should lie somewhere between the two undesirable error extremes. With the optimum relationship, test error will decrease as the model complexity increases. Other issues related to overfitting are dealt with in [39–40].

To allow an estimation of the test error E_d , which is also sometimes called the perceived noise σ_v , it is assumed that the experimental data is accurate and the errors are calculated by making a comparison between the predicted output (y_j) and the experimental data (t_j).

$$\text{with, } E_d \propto \sum_j (t_j - y_j)^2$$

A problem associated with using best fit functions (or inserting best fit weight) is that the model may not accurately estimate uncertainties where data is scarce or where data is noisy. To avoid this difficulty, a committee of models is formed to predict the output instead of using single models. The perceived noise arising from different models is plotted against the best models ranked in terms of test error. Committees are then formed that combine the predictions of the number of models L , with $L = 1, 2, 3, \dots$ etc. Within the plot of L versus the perceived noise, a minimum arises that shows the optimum size of the committee. Once the optimum committee size is formed, the complete model is retrained on the entire data to allow some minor adjustments on the weights. Additional information about the advantages of using a committee of models is presented in [41]. A brief look will now be taken at some results generated from four models that were created.

4.1.4 Neural Network Predictions

At University of Cambridge four neural network models were constructed to predict impact toughness, yield strength (YS), ultimate tensile strength (UTS) and elongation percentage (Elong) based on a database of some 3300 experimental weld metal results. The input variables of the models are presented in Table 4 of Paper 1 [Appendix]. The experimental data within the database was generated from different types of arc welding - SMAW, SAW and TIG. As previously stated, a committee of models gives better predictions and as a result an assessment was made for the optimum size of committee. The results of this assessment for each mechanical property are presented in Table 4.1

On the basis of Lord's work [21], a base composition was chosen as presented in Table 4.2, to generate a contour plot of impact toughness behaviour at $-40\text{ }^{\circ}\text{C}$ as a function of Mn and Ni concentrations. The resultant contour plot of the predicted toughness and uncertainty is shown in Figure 4.4. Given the results obtained in Figure 4.4 which are fully discussed in Papers 1 and 7 in the appendix, it was decided to set Ni at 7 wt. % and Mn at 0.5 wt.%. It was decided to continue the modelling for other alloying elements and C additions both as a function of strength and impact toughness at $-60\text{ }^{\circ}\text{C}$ proved to be interesting. It was predicted that strength could be increased at moderate expense to impact toughness with small additions of carbon. The generated plots are shown in Figures 4.5 and 4.6. and are fully discussed in Paper VII, Appendix.

Additional predictions were made to see the effects on toughness at $-60\text{ }^{\circ}\text{C}$, by varying the concentration of alloying elements such Cr, Mo, Ni, N, Si, and B. Also the effect on impact toughness at $-60\text{ }^{\circ}\text{C}$ was modelled by changing heat input with respect to interpass temperature. These latter plots were not as dramatic for mechanical properties and may be found in Figures 9–11 of Paper I, Appendix. This work needs to be

Model	No. of members in committee	σ_{ν} (Perceived noise)
Toughness / J	5	0.055
YS / MPa	13	0.025
UTS / MPa	5	0.02
Elong / %	2	0.05

Table 4.1 Showing some of the basic model characteristics.

C	0.034	Mo	0.62	N / ppm	250
Mn	0 - 2	V	0.011	B / ppm	1
Ni	0 - 12	Cu	0.04	Nb / ppm	10
Si	0.25	Co	0.009	HI / kJ mm^{-1}	1
S	0.008	W	0.005	IPT / $^{\circ}\text{C}$	250
P	0.01	O / ppm	380	PWHT / $^{\circ}\text{C}$	250
Cr	0.5	Ti / ppm	80	PWHT / h	16

Table 4.2 Base composition and parameters used for analysing the effect of Mn and Ni concentration on toughness at $-40\text{ }^{\circ}\text{C}$. All elements are in wt. % unless otherwise specified [Paper 1, Appendix]. HI is heat input, IPT is interpass temperature and PWHT is post weld heat treatment. The term PWHT in these calculations refer to a degassing treatment.

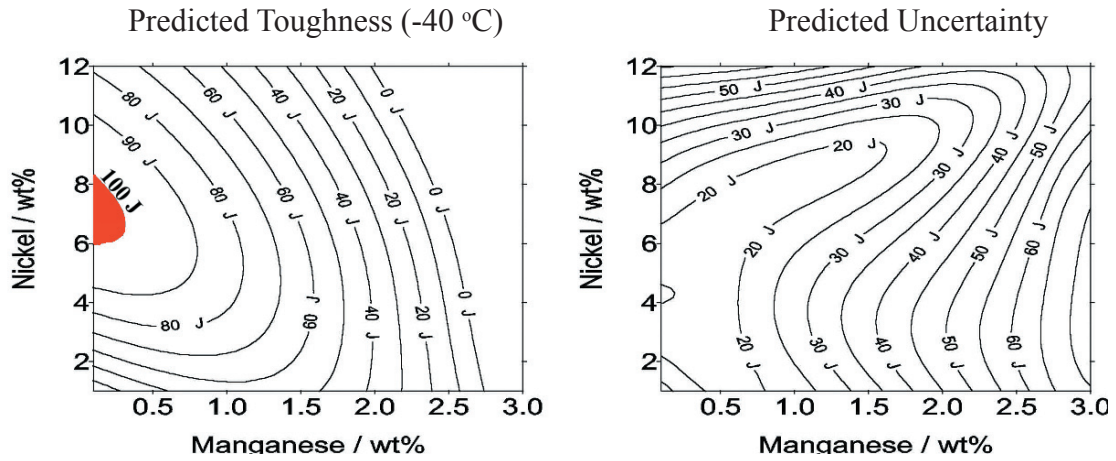


Figure 4.4 Contour plots showing the predicted weld impact toughness at $-40\text{ }^{\circ}\text{C}$ as a function of manganese and nickel concentration. The predicted uncertainty represents $\pm 1\sigma$ of uncertainty, [Paper I, Appendix].

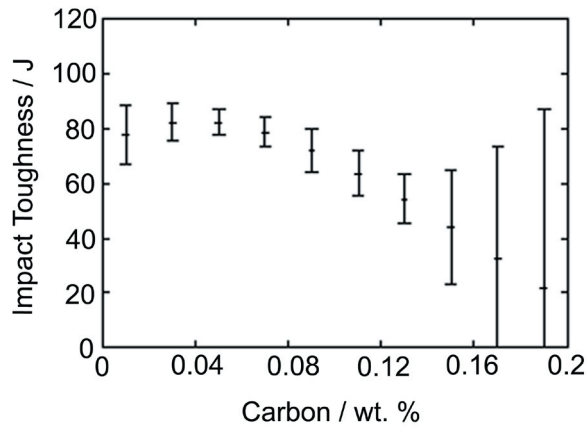


Figure 4.5 Predicted impact toughness at $-60\text{ }^{\circ}\text{C}$ as a function of carbon concentration. The error bars represent $\pm 1\sigma$ of uncertainty. [Paper VII, Appendix]

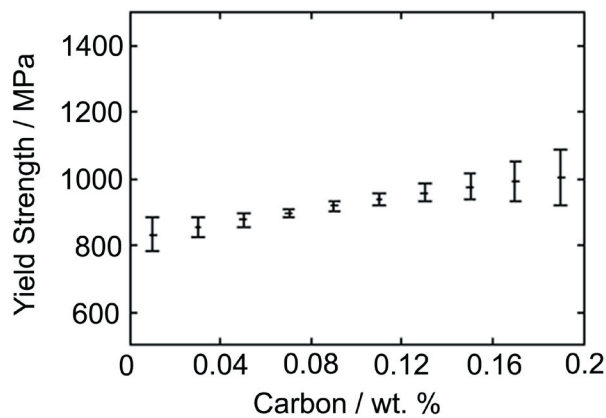


Figure 4.6 Predicted yield strength as a function of carbon concentration. The error bars represent $\pm 1\sigma$ of uncertainty. [Paper VII, Appendix]

continued and further developed changing the base input composition and welding parameters.

4.2 Thermodynamic Modelling

Work on calculating phase diagrams from expressions for the Gibbs free energy of phases in the system (the “CALPHAD” method) started in the 1970’s. One example is the Thermo-Calc software package which has been developed at the Royal Institute of Technology, Stocholm, Sweden where work started in 1976 [42–43]. The software was developed with the purpose of modelling all kinds of thermodynamic and phase diagram calculations. Like all modelling packages the software is strongly dependant on its databases to produce realistic simulations. There are many databases developed for specialised applications such as steels, slags, ceramic systems, electronic materials etc. These databases are continously being updated from an international network such as the Scientific Group Thermodata Europe collaboration.

Thermo-Calc is basically able to handle a variety of models which are used to describe the thermodynamics of different types of phases and the interface allows the user to calculate many different types of equilibria and obtain diagrams of various types. In this work Thermo-Calc was engaged to produce isopleths and to simulate the solidification using the Scheil-Gulliver model.

4.2.1 Solidification simulation

Thermo-Calc is mainly intended for equilibrium calculations but it can also be used to simulate transformations where local equilibria is concerned. The Scheil-Gulliver model uses this approach to simulate solidification. With this model it is assumed that the liquid phase is always homogeneous whereas the solid phases retains the composition it had when it formed. In other words the diffusion coefficients are equal to infinity in the liquid and equal to zero in the solids. At the interphase between the solid and the liquid it is assumed that conditions can be described by equilibrium thermodynamics [43].

In this work, the Scheil-Gulliver model was applied to simulate the solidification of the weld metals using the CCTSS database as a function of alloying content. Further details and results may be found in Paper VII, Appendix.

5. Experimental Details

5.1 Production of Experimental Weld Metals

5.1.1 The welded joint

The technique of Shielded Metal Arc Welding (SMAW) was employed to produce all experimental weld metals analysed in this work. The set up principles of SMAW welding are shown schematically in Figure 2.1. Welded joints were made according to ISO 2560 using 20 mm plates with a backing plate as shown in Figure 5.1. The joints were 'buttered' prior to welding which involved the deposition of two layers of weld beads along the joint edges of the plates. The deposition of the experimental weld metals took place in 33 cm runs with two or three runs per layer. This particular joint geometry gives very limited dilution of the weld metal and allows accurate evaluation of the weld metal properties. A photograph of one of the welded joint cross-sections is shown in Figure 5.2.

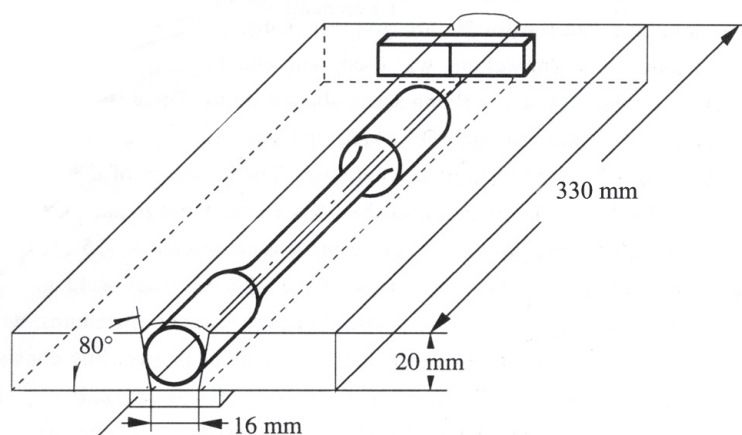


Figure 5.1 Schematic drawing showing the weld joint geometry. The positions of the tensile and Charpy test specimens are also shown, however they are not to scale [45].

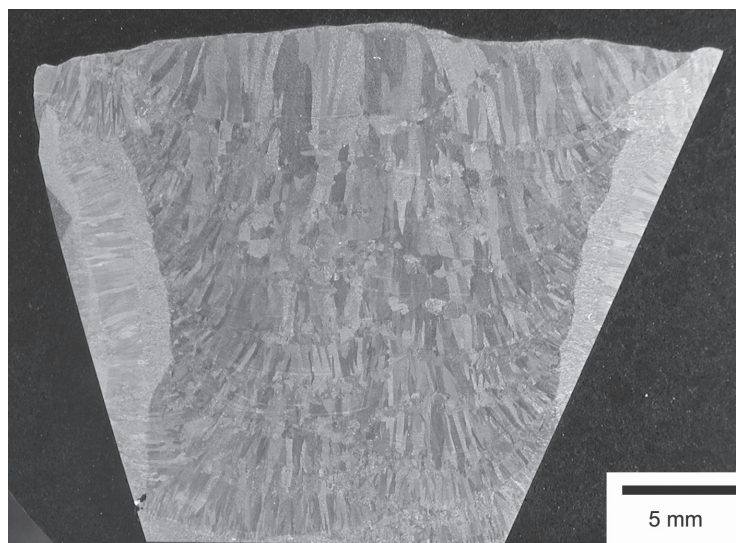


Figure 5.2. Macro photograph of the 7-2L250 welded joint cross-section.

5.1.2 Compositions and welding parameters

Experimental weld metal compositions were chosen based on results from the neural network modelling as already stated. On completion of the welding, a chemical analysis was performed on each of the new weld metals. Samples of weld metal were removed from the joint cross section, perpendicular to the welding direction and analysed using a Spectro Lab S optical emission spectrometer and Leco combustion equipment (Model EF 500 for C and S and model TC - 436 DR for N and O). The results from these analyses, giving the weld metal compositions, along with welding parameters are presented in Table 5.1. It was decided to name the weld metals according to their alloying content and welding procedure for ease of the reader. In weld metal 7-2L250, 7 stands for nickel content, 2 is for manganese content, L indicates low carbon content of approximately 0.03 and 250 indicates interpass temperature.

	7-2L250	9-2L250	7-0.5L250	7-0.5L200	9-0.5L200	7-0.5M200	7-0.5H200
E / kJ mm ⁻¹	1.2	1.2	1.0	1.3	0.7	1.4	1.3
I.P.T. °C	250	250	250	200	200	200	200
t _{8/5} / s	12	11	10	10	5	11	10
C *	0.032	0.031	0.024	0.030	0.026	0.061	0.110
Mn	2.02	2.11	0.64	0.61	0.37	0.56	0.53
Ni	7.23	9.23	6.6	6.11	8.67	6.84	7.04
Cr	0.47	0.48	0.21	0.16	0.2	0.15	0.14
Si	0.25	0.27	0.35	0.4	0.34	0.34	0.38
S*	0.008	0.008	0.008	0.009	0.008	0.006	0.007
P	0.011	0.011	0.012	0.010	0.007	0.011	0.008
Mo	0.63	0.64	0.4	0.38	0.41	0.35	0.40
O / ppm*	380	340	400	340	367	350	260
N / ppm*	250	260	197	150	130	160	100
V	N.A.	N.A.	N.A.	0.018	N.A.	0.014	0.016
Cu	0.03	0.03	0.03	0.02	0.01	0.01	N.A.

Table 5.1 Welding parameters and chemical composition. Welding parameters presented are energy input (E), interpass temperature (I.P.T.) and the estimated cooling time between 800 and 500 °C (t_{8/5}) calculated from [14]. Composition is in wt. % unless otherwise stated, N.A. is not analysed and ‘*’ indicate elements analysed using Leco Combustion equipment. No post weld heat treatment was carried out.

5.2 Mechanical Investigations

5.2.1 Tensile testing

Tensile testing can be used to access several mechanical properties of the weld metal. In this work, specimens were deformed until fracture by increasing the tensile load uniaxially along the axis of the specimen. The specimens were machined longitudinally from the weld deposits as shown in Figure 5.2. The specimens had a length of 115 mm, a diameter of 10 mm and a gauge length of 70 mm. Elongation was measured over 50 mm. Tensile testing was performed in compliance with standard EN 10045-1.

5.2.2 Charpy impact testing

Charpy V-notch testing is used to measure the impact energy which is sometimes also termed the notch toughness [46]. For Charpy testing, transverse specimens were machined in the shape of a bar having dimensions 10 mm × 10 mm × 55 mm, as shown in Figure 5.1. These were then notched in the weld metal centre perpendicular to the welding direction, with a notch depth of 2 mm and a total notch angle of 45°. Two or three specimens were tested at each temperature. Charpy impact testing was performed in compliance with standard EN 10045-1.

5.2.3 Hardness testing

Hardness is a measure of the weld metal's resistance to localised plastic deformation. Hardness testing was conducted according to Vickers method using a 10 kg load with a Buehler hardness tester on joint cross-sections polished to 1 µm with diamond paste. Samples were hardness tested starting in the last bead and then proceeding vertically down the weld metal cross section in 1 mm steps. In total 16 indentations were made on each weld metal. Hardness testing was also carried out using Vickers method with a 1 kg load on dilatometry specimens polished to 1 µm with diamond paste. All hardness measurements were carried out in agreement with standard EN 11 25 17.

5.3 Microstructure Characterisation Techniques

5.3.1 Light optical microscopy (LOM)

Light Optical Microscopy is one of the most commonly used techniques for microstructure characterisation in the development of weld metals. Steel weld metals are opaque to visible light and as a result only the surface of the weld metal sample is subject to investigation with this technique. The image contrast is a result of variations in reflectivity in the different regions of the microstructure. Limitations of this technique are its spacial resolution at approximately 0.5 µm and its depth of field. Investigations in this work was carried out using a Leitz Aristomet light optical microscope.

5.3.2 Scanning electron microscopy (SEM)

The scanning electron microscope is a widely used instrument to obtain information on bulk specimens. In this work, a Philips XL30 high / low vacuum scanning electron microscope was used for low magnification analyses while a Leo Ultra 55 FEGSEM was used to carry out investigations of high magnifications. A schematic drawing of a conventional SEM representing the Philips XL30 is shown in Figure 5.3 while in Figure 5.4 a schematic of the Leo Ultra 55 FEGSEM is presented.

The main task of the electron gun is to provide a stable beam of electrons with adjustable energy. There are several types of electron guns available and these are mainly categorised by their ability to produce an amount of current into a small spot, the stability of the emitted current and the lifetime of the source. The Philips XL30 SEM was fitted

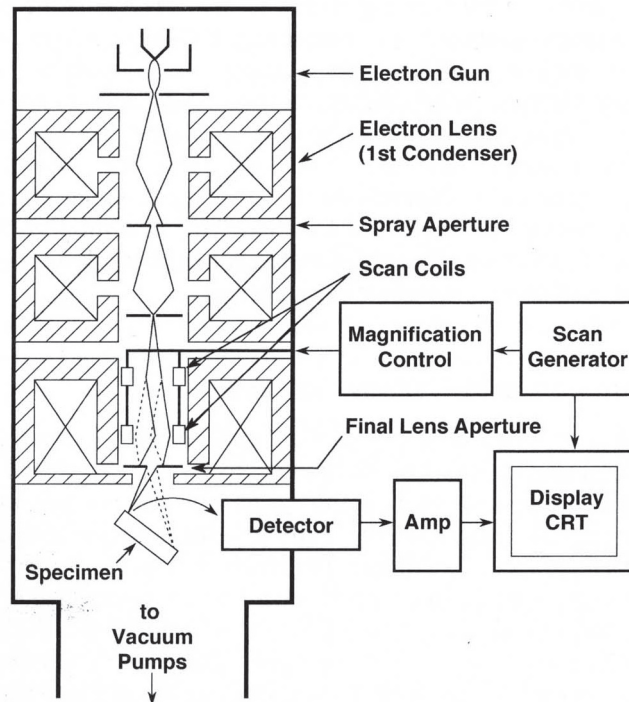


Figure 5.3 A schematic drawing of the electron column showing the electron gun, lenses, the deflection system and the electron detector. [47]

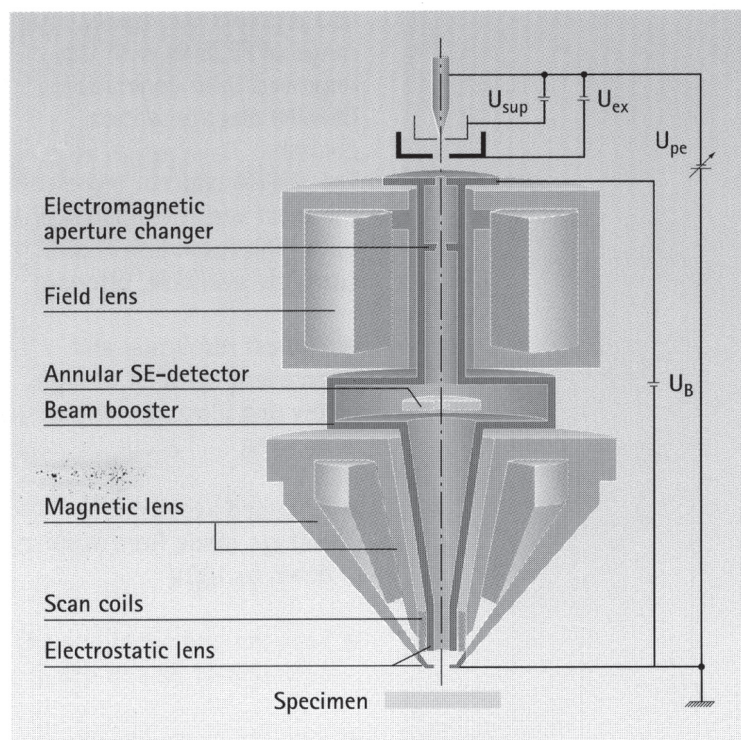


Figure 5.4 A schematic drawing showing the operating principle of the Leo field emission column. U_{pe} - tip voltage (final energy of the electron beam), U_{ex} - extractor voltage at the first anode, U_B - booster voltage at second anode. [48]

with a tungsten thermionic emitter while the Leo Ultra 55 FEGSEM had a Schottky field emission source.

The tungsten thermionic emitter is fairly reliable and inexpensive and is commonly used for low magnification imaging. A schematic is shown in Figure 5.5. The tungsten wire acts as cathode and is about 100 μm in diameter bent into a V shaped hairpin. The filament is heated resistively by a current to about 2500 K and as a result thermionic electrons are emitted. The electrons spread out in the form of a cone while the Wehnelt cylinder acts to focus the electrons and control the amount of emission. Lines of constant electrostatic field potential or equipotentials are also shown in Figure 5.5. The electrons move towards the positive potential so that they leave the filaments only where the positive electrostatic field lines meet the surface of the filament. The emitted electrons are focused into a crossover which is given by the high curvature in the equipotentials near the hole in the Wehnelt cylinder due to the bias voltage. The emitted electrons are accelerated from the negative potential of the filament to the ground potential of the anode. The anode contains a small hole which allows a fraction of the electrons to proceed down the column while those collected by the anode are returned to the high voltage power supply. [47]

The field emission gun usually uses a cathode in the form of a wire shaped into a sharp point (tip radius 100 nm or less) which is supported by a tungsten wire in the shape of a hairpin. An electric field is concentrated at the tip when a negative potential is applied to the cathode. The field is mainly applied to reduce the effective work function barrier. To lower the work function barrier even more ZrO_2 is deposited on tip of the cathode. This extra doping of the surface gives the result that the brightness and emission density is very high. Additionally, the filament is heated to about 1800 K to keep it clean which reduces noise and instability. The voltage between the first anode and the tip determines the field strength available to extract electrons and it is usually between 3–5 kV. The voltage difference between the tip and second grounded anode determines the acceleration voltage of the gun which can be between a few hundred volts and 30 kV. A schematic of the Schottky gun is shown in Figure 5.6. [47–48]

Once the electrons enter the column they are controlled by electromagnetic lenses as shown in Figures 5.3 and 5.4. The Philips XL30 SEM was fitted with conventional lens systems. The column is fitted with both a condenser lens and an objective lens. The main task of the condenser lens is to demagnify the electron beam for a particular imaging mode. The objective lens gives further demagnification and focuses the electron probe onto the sample. The column of the Leo Ultra 55 FEGSEM is unique in its design. It is fitted with a beam booster which maintains a high beam energy through the column regardless of the electron beam energy selected. Once the electron beam has passed the scanning system it is decelerated to its final landing position on the speci-

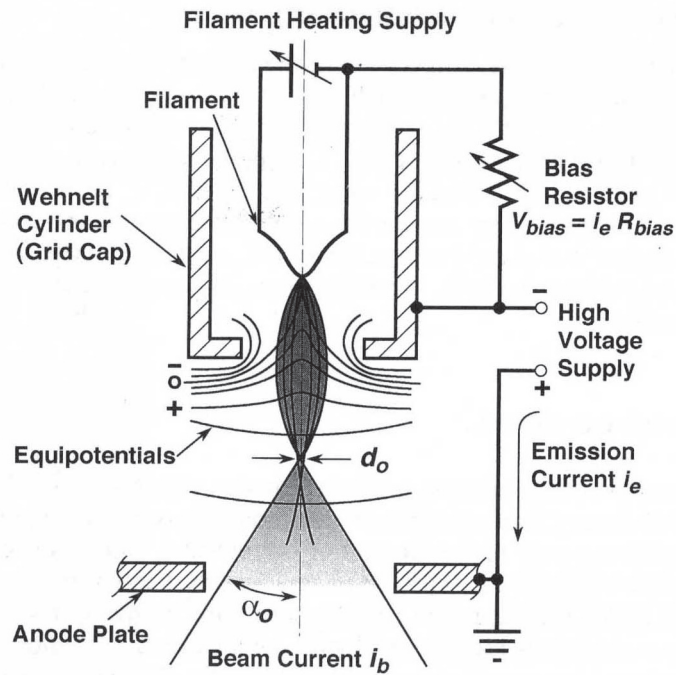


Figure 5.5 A schematic drawing of a conventional self bias thermionic tungsten hairpin electron gun. [47]

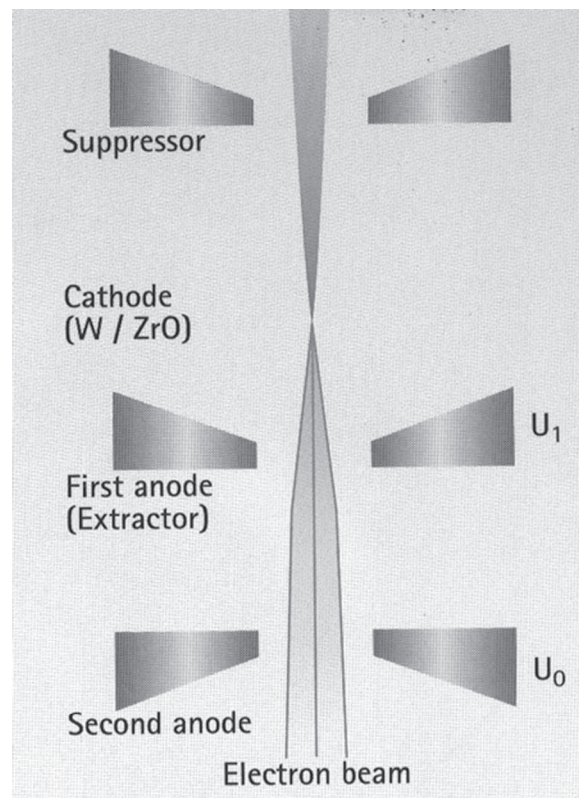


Figure 5.6 A schematic drawing of the scottly field emission source. [48]

men. The beam path in this instrument has been designed so that the beam crossover is avoided between the source and the specimen. An electromagnetic aperture changer is placed close to the gun and this in combination with the field lens select the optimum beam aperture angle and tune the probe current. The net effect of the high beam energy and cross-over free electron beam path is to minimise the statistical coulomb interactions between the beam electrons that normally leads to a reduction in brightness and limits the resolution. [47–48]

As the beam interacts with the specimen, different signals are generated that can be detected and collected which are used to form an image. The image formed is displayed on a cathode ray tube (computer monitor) at the same scanning rate as the electron beam scans the specimen [49].

The electron beam - specimen interaction volume is shown schematically in Figure 4.7. All signals generated are emitted simultaneously and each carry different information. Both Secondary electrons (SE) and Backscattered electrons (BSE) are used for imaging while X-rays are used for chemical analysis.

SE are generated as a result of interaction and transfer of energy of both incoming primary electrons and outgoing backscattered electrons with atoms within the material. SE have low energy, approximately less than 50 eV, and as a result come from the outer surface of the material from where they have enough energy to escape. The depth of examination depends on the beam energy, but normally SE come from depths between the surface and 5 ~ 50 nm. Additionally, their emission is effected by the inclination of the surface that leads to topographical contrast within the image.

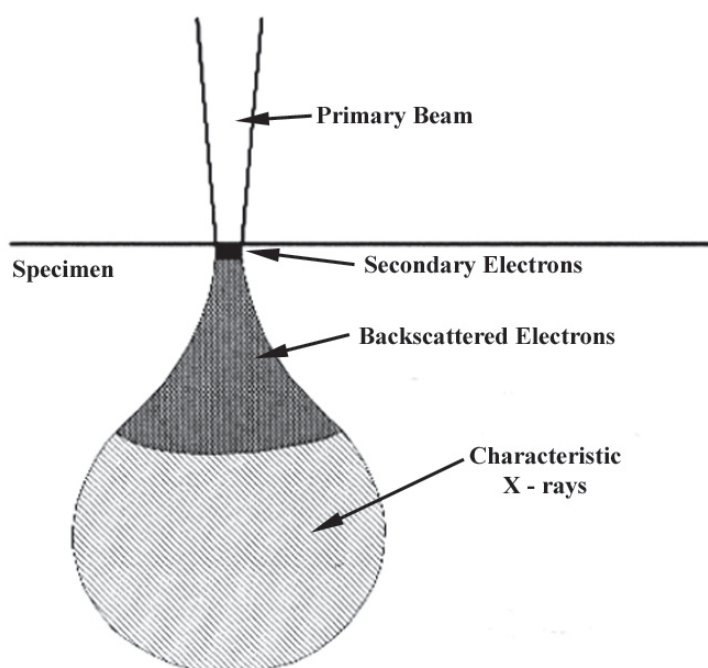


Figure 5.7 A schematic drawing of the beam - specimen interaction volume [50]. Secondary electrons come from the outer surface, backscattered electrons are coming from a larger and deeper area with characteristic X-rays having the greatest volume.

BSE are generated as a result of primary electrons coming from the electron beam that have been rebounded after collisions with the specimen. These have higher energy than SE, (greater than 50 eV) and come from a larger volume of the specimen (between the surface and 0.1 ~ 0.5 μm deep) as shown in Figure 5.7. BSE provide information on surface topography as well as atomic number contrast. The backscattering coefficient increases monotonically with Z and areas with a high average atomic number appear brighter in contrast. As a result, BSE provide information on compositional uniformity within the specimen [51]. Since both compositional and topographical contrast appear simultaneously, it is often difficult to interpret both combined. Greater knowledge from compositional contrast is gained when investigations are performed on flat surfaces.

Additional to SE and BSE, radiation in the form of X-ray photons is generated. This radiation provides chemical information when analysed using energy dispersive X-ray spectrometry (EDX). This will be dealt with in greater detail in Section 5.3.5.

An important point to note is that shape and size of the interaction volume affect the spatial resolution. Investigations with BSE and X-rays was only carried out with the Philips XL30 instrument while SE imaging was carried out on both the Leo Ultra 55 and Philips XL30. With the Philips XL 30, a common Everhart-Thornley SE detector was used and imaging with a resolution in the order of 5 nm is possible. However, with EDS the resolution can be as low as 1 μm . The limitations of spatial resolution is an important factor that must always be considered when interpreting and comparing results obtained from SE, BSE and X-rays. SE imaging on the Leo Ultra 55 was carried out using its characteristic In-lens SE detector which offers very high resolution (1.5 nm at 2.5 keV). Basically with this detector the secondary electrons generated at the impact point are collected by the decelerating field of the Beam Booster and accelerated through the objective lens upwards to the Inlens Secondary Electron Detector. The inlens secondary electron detector is best used at short working distances and it was optimised for a working distance of 2 mm in the instrument used. [48]

5.3.3 Secondary ion mass spectrometry (SIMS)

Dynamic mode secondary ion mass spectrometry allows the determination of lateral and in-depth concentration distributions of elements or their isotopes in layers up to several microns in thickness. In the course of the analysis, the sample is continuously sputtered which in turn leads to evaporation of the sample. This offers sensitive information that can be utilised to provide in-depth profiling or elemental mapping. In this study only elemental mapping was carried out.

Sputtering of the sample was carried out using a beam of primary ions of O_2^+ that were generated using a plasma discharge. The ions were accelerated and focused onto the specimen with a beam impact area of 200 x 200 μm . The impact of the beam results

in the evaporation of the outer atomic layers, in the form of secondary particles. A fraction of these are ionised both positively and negatively (see Figure 5.8). These ions are extracted into the mass spectrometer, using ion optics. The ion optics also control the size of the area analysed, the trajectories of the ions of separate energy and the kinetic energy range of the allowed ions [52]. The secondary ions emitted into the mass spectrometer possess a specific mass to charge

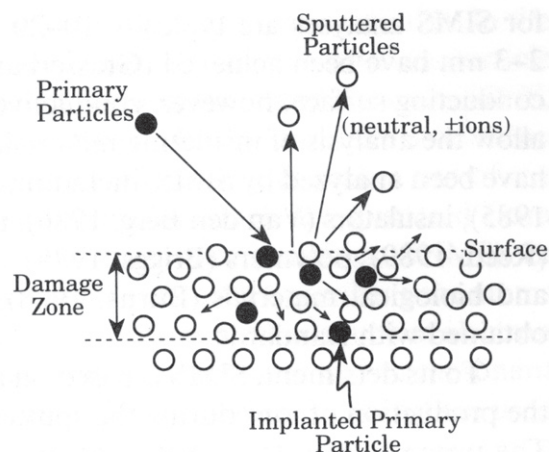


Figure 5.8 The sputtering process of SIMS showing the initiation of the collision cascade and the removal of material from the sample surface [51].

ratio within defined intervals of kinetic energy and also have a specific angle of emission. They are collected as in depth or along surface profiles, or as distribution images of the sputtered surface showing the selected element of specific energy [51].

5.3.4 Transmission electron microscopy (TEM)

TEM was used to analyse the microstructure on a finer scale. With TEM, knowledge was gained both about the microstructural morphology through imaging at high magnification (with resolution down to 0.5 nm or less attainable), and crystallographic information through electron diffraction. All investigations were carried out using 200 kV either with a Jeol 2000 FX TEM or a Philips CM200 FEGTEM.

In principle, the TEM can be split into different components; the radiation source, the illumination system, the image formation system and the projection system, as shown in Figure 5.9. Magnetic lenses are used to deflect the beam and these lenses behave in a similar manner to optical glass lenses. The illumination system transforms and projects the electron beam onto the specimen. The specimen must be thin, typically less than 100 nm, to allow transmission of the electrons. As the beam interacts with the specimen, different signals are generated as shown in Figure 5.10 and these will be discussed later. Within the image formation system, the first image formed is by the objective lens. This image is further magnified and projected onto the fluorescent screen using the projector lens system.

Figure 5.11 shows an electron beam undergoing transmission in a number of specific directions as a result of diffraction arising from parallel planes within the crystal which fulfill Bragg's law due to their orientation in relation to the incoming beam. Transmitted parallel beams are refracted into one spot in the back focal plane of the objective

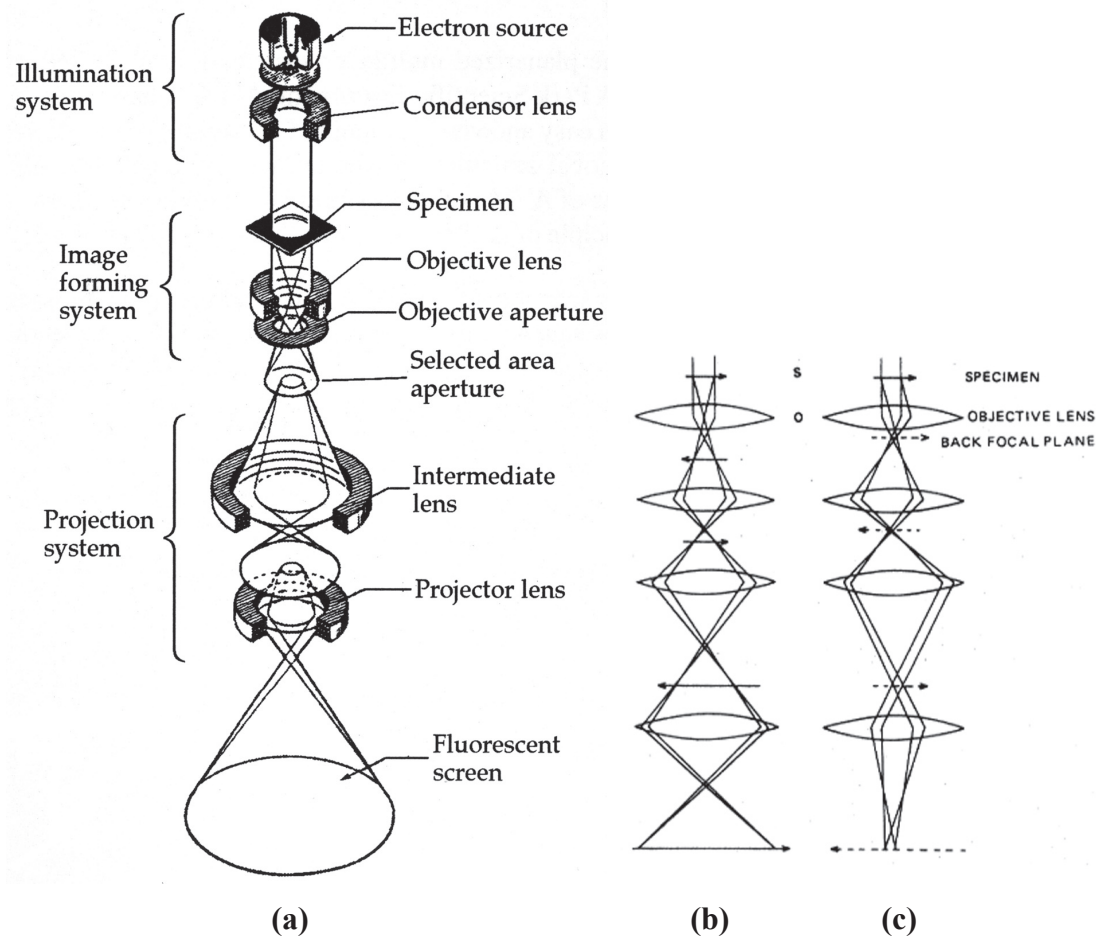


Figure 5.9 The basic principles of the TEM microscope (A). [Ref. 53, with some modifications.] Ray diagrams for imaging (b) and diffraction (c). [68]

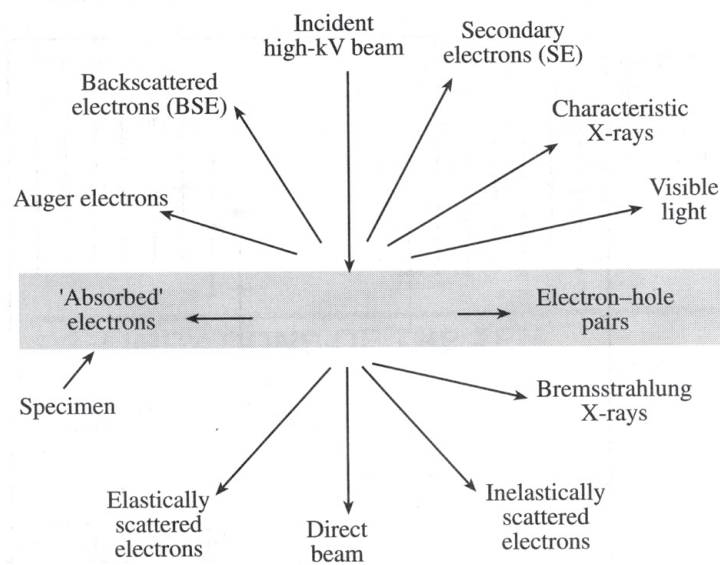


Figure 5.10 The signals generated as a result of the interaction between a high - energy electron beam of electrons and a thin specimen [Ref. 55].

lens. The beam diffracts in many directions and as a result spots in other lateral positions are formed on the focal plane. When all spots are taken into account, a diffraction pattern is formed. When the microscope is in diffraction mode, the focal plane of the objective lens is projected on to the viewing screen as shown in Figure 5.9c. The diffraction pattern can be indexed where the spots formed are attributed to different families of projecting planes. This is carried out by measuring both the angular relationships along with the distances between the spots in the pattern, and coupling this information with the beam energy and camera length. From the diffraction patterns, the structure and lattice parameters can be determined, that allow phase identification.

When the objective aperture is inserted in the back focal plane of the objective lens, the image contrast is determined by whether the central or a diffracted beam is allowed through. A bright field image is formed when the central beam passes through the objective aperture (Figure 5.11A) and a dark field image is formed when a diffracted beam is allowed through (Figure 5.11B and C). Figure 5.11C shows when the incoming beam is tilted so that the diffracted beam takes a central path through the microscope which reduced spherical aberrations within the image [55–57].

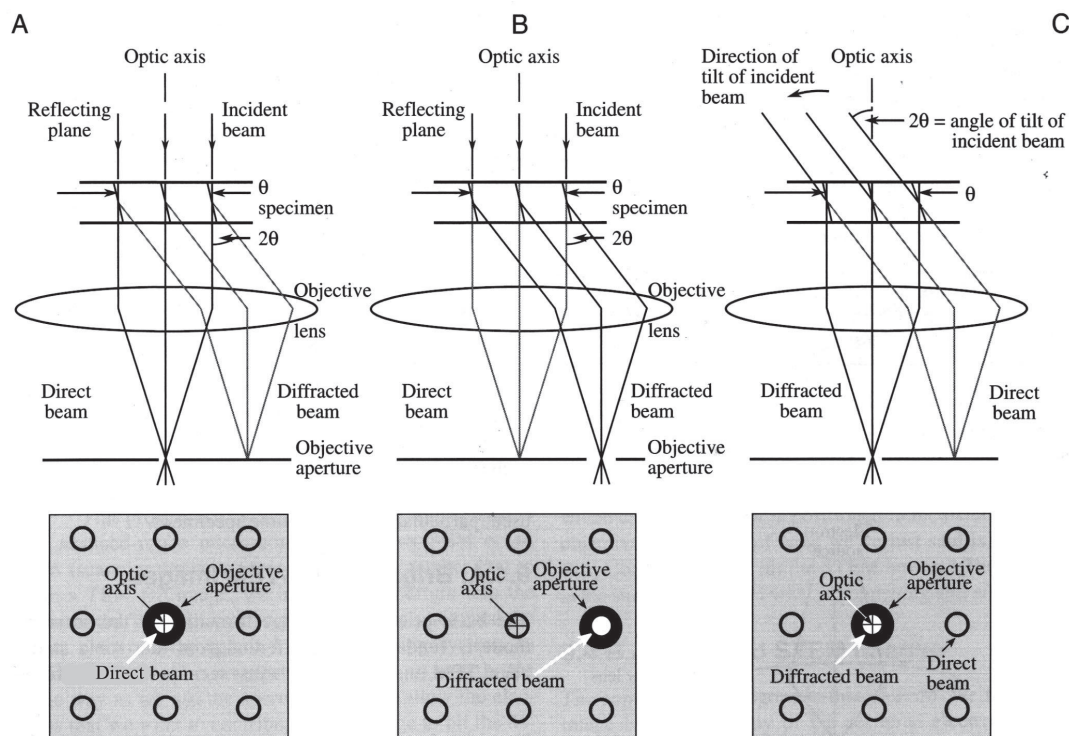


Figure 5.11 Ray diagrams showing how the objective lens / aperture are used in combination to produce (A) a bright field image formed from the direct beam (B) a displaced aperture dark field image formed with a specific off-axis scattered beam, and (C) a centered dark field image where the incident beam is tilted so that the scattered beam remains on axis. The area selected by the objective aperture as seen on the viewing screen, is shown below each diagram. [55, with minor corrections]

As was already stated when the beam hits the specimen (shown in Figure 5.10), it is split into a number of discrete directions as a result of its interaction with the crystallographic planes and additionally there are a number of secondary signals given off. Many of the secondary signals are used in analytical electron microscopy. One example, the generation of X-rays can be used in EDS analysis and provides chemical information about the specimen or features within the specimen. This will now be discussed.

5.3.5 Energy dispersive X-ray spectrometry

As already seen in both the SEM and TEM, the bombardment of a specimen with an electron beam leads to the generation of X-rays. These may be used to determine the elemental composition of different regions or features within the specimen. Investigations were carried out using a Link spectrometer.

Basically, electrons in the inner shells of an atom are ejected and the atom is ionised. The excited atom returns to its stable state by an electron in one of its outer shells releasing its excess energy in the form of X-rays and filling the hole. The emitted X-rays have a characteristic energy for the shells involved in the activity and are characteristic of the given element. They may be used to gain chemical information about the specimen.

The X-rays can be detected by a Si crystal which produces electrical pulses with an amplitude proportional to the energy of the incoming photon. The pulse amplitudes are measured and then stored in a multichannel analyser where each channel corresponds to a certain interval of pulse heights. A spectrum is then plotted showing the number of counts per energy channel. Peaks which form at certain energy levels in the spectrum can be identified and are proportional to the element(s) present within the specimen with that X-ray energy. The concentration of a given element can be determined by carrying out a quantitative analysis.

5.3.6 Atom probe field ion microscopy

Atom Probe Field Ion Microscopy (APFIM) has the highest resolution of all microstructural characterisation techniques in that lateral and depth resolution less than 1 nm can be attained simultaneously. The big advantage of APFIM is that single atoms are analysed and all elements are possible to investigate. The real benefit of applying APFIM in my work was that the carbon content was accurately measured and firm evidence was attained of the individual phases present in the microstructure.

An APFIM specimen is in the shape of a needle with a tip radius of maximum 50 nm. The specimen is placed in a vacuum chamber which is filled with a noble gas, neon in this work, at a pressure of 7×10^{-3} Pa, to allow imaging. A phosphor screen at ground potential is located a few centimetres (distance adjustable), in front of the specimen. A very high electric field is applied to the needle tip by placing a high positive voltage on the specimen. When an additional short higher voltage pulse is applied in the

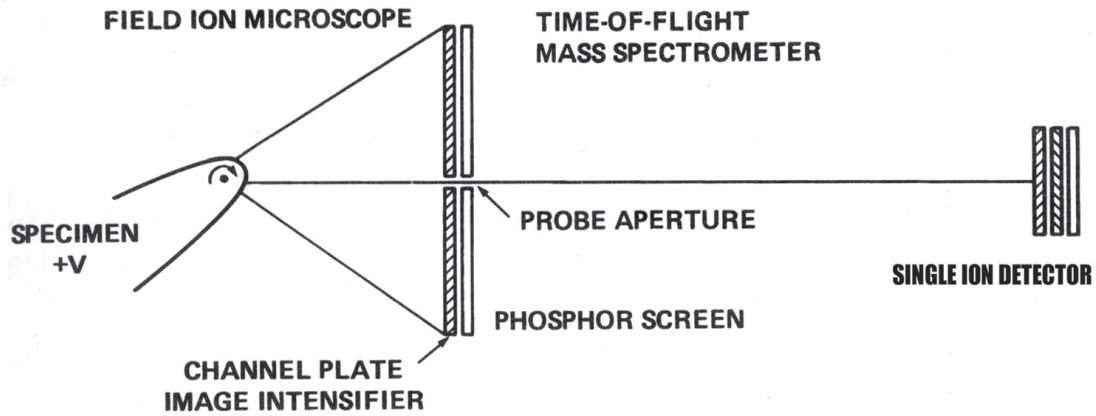


Figure 5.12. The basic principles of the atom probe, [Ref. 58, with some alterations]. The field ion microscope is on the left and the time-of-flight spectrometer is on the right. The probe aperture on the phosphor screen allows atoms in a selected area of the specimen tip to be analysed in the mass spectrometer.

order of nanoseconds, a process known as field evaporation may occur on the needle tip. This basically means that surface atoms on the needle tip are removed as a result of the applied field. Simultaneously the atoms become positively ionised and are repelled away from the needle in a radial direction. To ensure no field evaporation takes place between the high voltage pulses the specimen was cooled to cryogenic temperatures, between 50 and 70 K in this work. The evaporated atoms hit the earthed phosphor screen. Within the screen there is a small hole, shown in Figure 5.12 that serves as an analysing aperture and it only allows ions from a specific, chosen area on the specimen surface to enter a mass spectrometer. In order to make an analysis on a specific region, the specimen can be rotated until the image of that region falls over the aperture. Once the operator is satisfied with the instrument setup, the image gas is pumped out and the vacuum pressure is kept below 7×10^{-8} Pa. An evaporation pulse amplitude of 20 % of the standing voltage was applied to cause further field evaporation. The mass of the evaporated atoms is identified by time of flight spectrometry. The flight times of the atoms that pass through the hole and arrive at the detector are measured electronically. The mass to charge ratio is calculated from the equation:

$$m / n = (2eVt^2) / d^2 \quad (\text{Eqn. 5.1})$$

Where m/n = the mass to charge of the n^+ ion
 e = the electron charge V = specimen voltage
 t = time of flight d = the flight distance.

The APFIM instrument and evaluation system used in these investigations is further described elsewhere [59–61].

5.3.7 X-ray diffraction

X-ray diffraction measurements were carried out in Cambridge to measure the amount of retained austenite within the weld metal. A schematic drawing of a X-ray diffractometer is shown in Figure 5.13 and detailed descriptions of the method are available elsewhere, [62–63].

In brief, a sample is irradiated by monochromatic X-rays, which will be diffracted according to Bragg’s Law. There are a few possible sources, but most commonly used in crystallography are Cu- K_{α} or Cr- K_{α} . The diffraction intensity is measured continuously during a detector scan of 2Θ , coupled to a specimen rotation of Θ as shown in Figure 5.8. The recorded results are presented in the form of a diffractogram where I, the intensity, is plotted as a function of 2Θ . The recorded results are then compared with theoretical calculations and literature, Table 5.2, [63].

In this work, a Cu- K_{α} source was used with wavelength, $\lambda = 0.15418$ nm. The samples were measured in the 2Θ range, from 47 to 130°. The austenite content was measured using three peaks in the spectrum corresponding to the austenite plane (002), (022) and

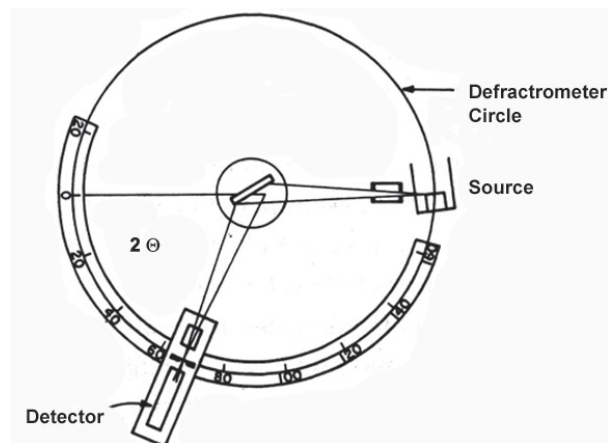


Figure 5.13. The basic principles of an X-ray diffractometer (65)

Θ angle	intensity %	h	k	l
43.473	100	1	1	1
50.674	80	2	0	0
74.679	50	2	2	0
90.676	80	3	1	1

Table 5.2 Expected X-ray diffraction data for austenite using a Cu- K_{α} source with wavelength, $\lambda = 0.15406$ nm, [63]. Θ angle, is the angle at which austenite peaks should occur in the spectrum, intensity %, is the percentage of the X-rays diffracted at the different angles from the atomic planes and h, k and l correspond to the plane index points in the (h,k,l) plane.

(113) to allow for texture effects. The measurements were made on samples taken from the cross section of the welded joint but the exact location of the sample was unknown. A computer program used in the quantification of the austenite from the diffractograms and can be found in [64].

5.3.8 Dilatometry

Dilatometry uses the characteristic of thermal expansion to characterise phase transformations occurring in a material. The dimension of a sample under negligible load was measured in the horizontal direction as shown in schematic in Figure 5.14 as a function of a given temperature cycle. The sample is held between two push rods which transmit the dimensional changes. These push rods act as an intermediary between the sample and the transducers that registers the change dimensions. The sample expands by a certain amount as shown by the shaded area ΔL_S . From looking at Figure 5.14 it is clear that there will be error in ΔL_S since portions of rods A and B are in the controlled environment and they themselves will expand on heating ΔL_A and ΔL_B . As a result the measured value of ΔL_S can be written as:

$$\Delta L_S = (\Delta X_A - \Delta L_A) + (\Delta X_B - \Delta L_B)$$

This means the value of ΔL_S cannot be determined from the measured values of ΔX_A and ΔX_B unless ΔL_A and ΔL_B are accurately accounted for in some way.

This was carried out by calibration using a standard where a well defined material was first ran and the combined values ΔL_A and ΔL_B is known and a “system correction” can be made. The standard usually has been tested by some other absolute method (such as twin telescopes, interferometer, etc) and is well defined. It is of critical importance that both the standard and the test sample are the same length. This makes the protruding lengths of rods A and B in the controlled environment identical both during the calibration and the during the test. In addition to the same length, the calibration thermal cycle must closely approximate the test cycle and the expansion of the reference must be close to the expected expansion of the sample.

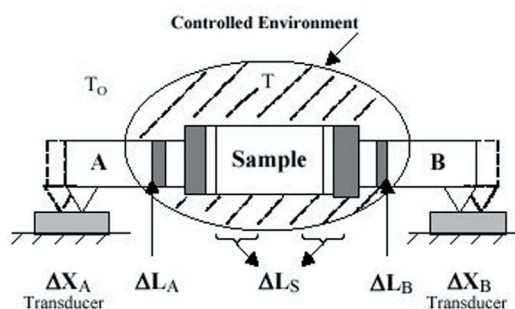


Figure 5.14 Principle of push rod dilatometer [66]

In this work a Theta Dilatronic III dilatometer was used which uses a horizontal configuration. Temperature was measured by attaching a thermocouple to the outer surface of the sample.

5.4. Specimen Preparation

5.4.1 LOM, SEM, SIMS and X-ray diffraction

Samples of weld metal for these investigations were taken from the joint cross-section perpendicular to the welding direction. In this way, the cross-section of the weld beads and their geometry were taken into account when carrying out microstructural investigations. The weld metal samples were mounted in conductive bakelite. These were then ground and polished to a mirror like surface. This was achieved by using successively finer abrasive paper and then polishing through 9, 6, 3 and 1 micron diamond paste on Struers polishing plates.

For LOM and X-ray diffraction investigations, the microstructure was revealed using 1% Nital (HNO_3 in $\text{C}_2\text{H}_5\text{OH}$) etchant. With SEM, investigations were carried out, both on polished samples and etched samples while only polished specimens were analysed using SIMS.

5.4.2 TEM

For TEM investigations, 3 mm disc shape specimens perpendicular to the welding direction were ground to between 50 and 80 μm . The discs were then jet electropolished using Struers Tenupol 3 equipment with 10% perchloric acid in methanol which was cooled to $-35\text{ }^\circ\text{C}$. The foils were thinned further using a Gatan precision ion polishing system (Model 691) at 3.5–4.0 keV at an angle of approximately 4.2° , for 3–4 mins.

5.4.3 APFIM

Atom probe field ion microscopy (APFIM) was performed on the last bead of weld alloys 1 and 3. Atom probe specimens were prepared by first removing a block of weld metal that included the last bead with approximate dimensions $10 \times 10 \times 15\text{ mm}^3$. The bead structure of the weld metal was then exposed by etching in ammonium-peroxodisulphate and photographed. The block was then subjected to electric discharge machining (EDM) using a Charmilles Isopulse Type P25 discharge machine. Cuts were made parallel to the welding direction in order to produce rods with approximate dimensions, $0.4 \times 0.4 \times 10\text{ mm}^3$. On completion of EDM, the sample was again photographed to allow the rod locations to be traced as shown in Figure 5.15.

Rods were then individually removed and electropolished to produce needle shape specimens with a tip radius of less than 50 nm using standard electropolishing methods [58]. The electropolishing was carried out in two steps as shown in Figure 5.16. In the

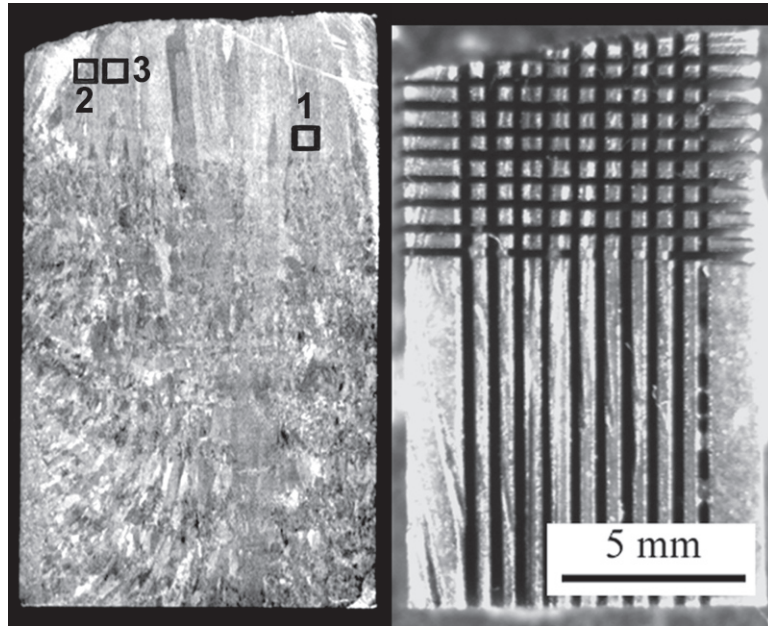


Figure 5.15 Macro showing weld metal from Alloy 1 with the bead structure exposed before, and the resultant rods after EDM. Also shown are the specimen locations for analysis 1 - 3 of Alloy 1 in Paper 3.

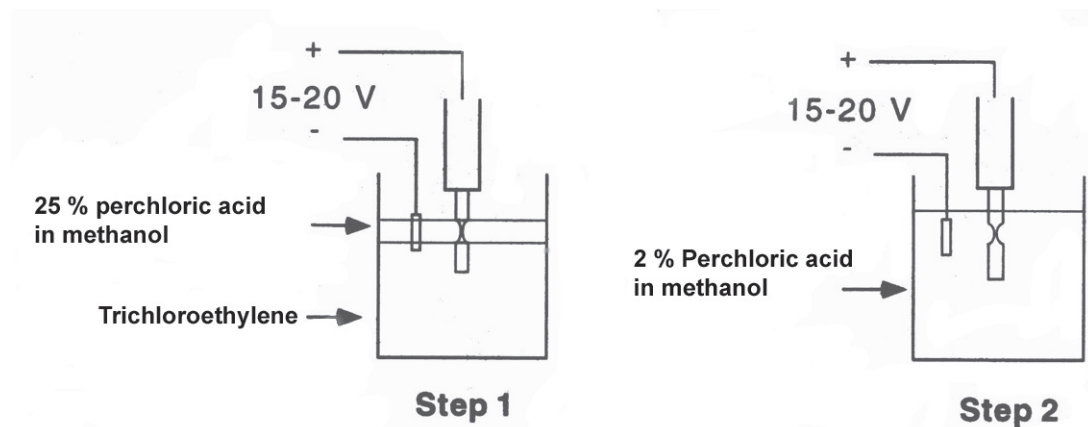


Figure 5.16. The two stage set up used to produce APFIM specimens by electropolishing [67, with some modifications].

first step, a neck was formed by placing the middle of the specimen in a 4–5 mm thin layer of electrolyte (30 % perchloric acid, 70% methanol) that was floating on a denser and chemical inert liquid, trichloroethylene. In the second step a weak electrolyte was employed (2% perchloric acid in 2-butoxyethanol) to allow a slower polishing rate. The polishing was carried out until the lower half of the specimen fell off, leaving a sharp needle. All specimens were first examined using TEM to observe the shape of the needle, and in some cases the specimen was further electropolished to enhance the specimen shape. This final electropolishing was carried out in the weaker electrolyte, applying short voltages pulses (10 V for 0.2–10 ms) which allows a controllable amount of material to be removed. The specimen was again examined with TEM and once satisfied with the specimen, it was inserted into the Atom Probe for analysis.

5.4.4 Dilatometry

Two types of cylindrical dilatometry specimen were used in investigations. For measurements greater than $50\text{ }^{\circ}\text{C} / \text{s}$ cooling tube type specimens were used. These had an outer diameter of 4.9 mm, an inner diameter of 3.5 mm and a length of 12.5 mm. The second type of specimen used for slower cooling rates ($< 50\text{ }^{\circ}\text{C} / \text{sec}$) were in the form of cylinders with a diameter of 3 mm and a length of 10 mm. All specimens were machined from the centre of the given welded joints.

6 Results and Outlook

This chapter makes a short summary of the results presented in the 9 appended papers. The most important aspects of each paper is highlighted. Some concluding remarks are made and an outlook for future work is given. For the reader with limited time a good overview of the main points is presented in Papers 7 and 8.

6.1 Summary of appended papers

A short description is given below of appended Papers I-IX. For detailed results, discussion and conclusions please see the papers in Part 2 of the thesis.

Paper I

Paper 1 presents the early approaches in the project to the problem of increasing strength while maintaining impact toughness in high strength steel weld metals. Neural network modelling was engaged and full details about the modelling are presented. Model predictions that suggested large impact toughness increases could be achieved as a result of reducing manganese at nickel levels of 7-9 wt. % were confirmed with the production of weld metals. Possible mechanisms for impact toughness increases were proposed.

Paper II

This paper presents initial results from studies of microstructure. It allows the reader to follow the progress and appreciate the complexity of the microstructures being studied. At this stage it was understood that segregation was an important factor and that the microstructure was a mixture of martensite and bainite.

Paper III

The different microstructural constituents found in a 7 wt. % Ni 2 wt. % Mn weld metal are investigated using a combination of LOM, FEGSEM and TEM. In addition a CCT diagram was constructed from the results of dilatometry measurements. A novel constituent with a large grain size was identified and characterised to be that of coalesced bainite. It was found that an inhomogeneous microstructure formed with mainly upper and coalesced bainite in former dendrite core regions while mainly martensite was found in interdendritic regions.

Paper IV

Using the composition of commercial electrode OK 75.78 as a base, the effect of nickel additions from 3 to 7 and 9 wt. % at manganese levels of 2 wt. % are investigated. It was found that nickel additions increase strength but decrease impact toughness. Investigations of the microstructure reveal that it changes from mainly that of lower bainite with 3 wt. % nickel to an inhomogeneous mixture of upper and coalesced bainite in

dendrite core regions with martensite at interdendritic regions at high nickel contents. The mechanical properties were discussed and explained in terms of the microstructure. Toughness loss was attributed to the formation of coalesced bainite at high nickel contents.

Paper V

This paper deals with the variation of manganese content at 7 wt. % nickel. Detailed microstructural studies were carried out with LOM, FEGSEM and TEM. It was found that the amount of coalesced bainite within the microstructure was reduced and replaced with upper bainite when manganese was changed from 2 to 0.5 wt. %. The large toughness gain as a result of manganese reductions was explained in terms of microstructure.

Paper VI

The effects on both the microstructure and properties of varying carbon between 0.03 and 0.11 wt. % were studied at 7 wt. % nickel and 0.5 wt. % manganese. It was found that carbon additions increased strength at moderate loss to toughness. Strength increases were attributed to the formation of greater amounts of martensite within the microstructure.

Paper VII

The most important results from the neural network modelling are presented. The effects of changing nickel, manganese and carbon content on the weld metal microstructure are summarised. Thermo-Calc is engaged and simulations of segregation behaviour during solidification are presented. It is concluded that all the weld metals solidify completely as austenite. Based on microstructural investigations a constitutional map (microstructure as a function of manganese and nickel contents) was constructed.

Paper VIII

The changes in the mechanical behaviour as a result of variations in nickel, manganese and carbon contents in the different weld metals are presented. The results are discussed in detail and explained in terms of microstructure.

Paper IX

The tolerance to variations in the weld thermal cycle of a 7 wt. % nickel weld metal were investigated. The mechanical properties were discussed in terms of microstructure and compared with those of a conventional 3 wt. % Ni weld metal for different welding conditions. It was found that strength and toughness was similar with both nickel levels at intermediate cooling rates, however there was less variation with welding conditions in the properties of the 7 wt. % Ni weld metal. It was concluded that high nickel levels offer advantages in terms of tolerance to variations in the weld thermal cycle.

6.2 Concluding remarks

Working with weld metals was challenging due to the inhomogeneity of the microstructure within the welded joints. It is important to have a good understanding of the microstructure in the as deposited last bead before the microstructure in reheated regions could be fully understood. This was necessary since there is always some uncertainty about what temperature each region has been reheated to during the multiple weld passes. Since the mechanical properties are normally measured in reheated regions, it is necessary to have a comprehensive understanding of the microstructure in these regions in order to be able to explain the mechanical properties.

In this project, extensive investigations with LOM were carried out to allow an overview to be obtained. Conventional SEM investigations were made but, it was difficult to interpret results due to limited resolution. Investigations with FEGSEM were very enlightening as to whether martensite, upper, lower or coalesced bainite existed. Also it was possible to investigate a large number of areas with good resolution relatively quickly. When FEGSEM results were combined with knowledge obtained from conventional TEM many interpretations could be made. From electron diffraction in combination with bright field and dark field TEM imaging it was possible to conclude what constituents existed within the microstructure. Comparing the images from TEM with FEGSEM micrographs, it was possible to conclude that the precipitates observed with FEGSEM were those of cementite for example. It was similar for LOM micrographs where martensite and bainite could be interpreted from knowledge obtained with FEGSEM.

Investigation with TEM was challenging since the specimens were magnetic and tilting within the microscope affected the electron beam and microscope alignment. In addition specimens needed to be prepared fresh before each TEM session since the specimens oxidised even when left in a desiccator.

6.3 Outlook

There are several interesting investigations remaining to be carried out in this project. The following are a number of key questions that would be interesting to answer:

Concerning coalesced bainite, it would be valuable to produce some test weld metals with different manganese and nickel contents in the region where B_s and M_s are predicted to be equal to each other in Paper VII. This work would confirm the role of B_s and M_s on the formation of coalesced bainite.

It would also be interesting to carry out energy filtered TEM on the cementite that forms in the bainite in these weld metals. With this technique it is possible to carry out elemental mapping and to see the complete distribution of cementite, all orientations at the same time, by filtering for carbon. In addition cementite at boundaries should be easy to distinguish from films of retained austenite. For example with 2 wt. % manganese many cementite platelets formed within the coalesced bainite while in 0.5 wt. % Mn weld metals only a few spherical precipitates were seen within the bainitic ferrite.

Applying the most promising weld metals in joints with high strength steel would be interesting. This work has been started to a limited degree in Paper IX but much work remains. The effects of dilution, lower interpass temperatures and different joint geometries need to be examined in greater detail.

Future work with neural network modelling investigating the possibilities of increasing strength while maintaining impact toughness would also be interesting. In this work, the base weld metal composition could be changed depending on results produced with other alloying elements and welding parameters.

7. Acknowledgements

There have been many people who helped me to reaching this far, my sincere thanks to the following people: -

My supervisors, Prof. Hans Olof Andrén and Docent. Leif Karlsson, for giving me this great chance in life. The stimulation and guidance I have received has been a dream. Our friendship has been a great source of joy for me.

Adjunct Prof. Lars Erik Svensson for sharing your vast experience of welding with me over the past year.

Prof. Harry Bhadeshia, for sharing your encyclopedic knowledge of steel and for your much valued comments on all my work.

Marimuthu Murugananth, for your computational work, our stimulating discussions and friendship.

Mattias Thuvander for fruitful discussions and for your interest in my work. Many thanks for running extra investigations parallel when time was limited.

Assoc. Prof. Lena Falk, for introducing me to the TEM.

Adjunct Prof. Jan Olof Nilsson, for giving me the opportunity to visit Sandvik Steel in order to carry out dilatometry and microscopy when needed.

The present and past staff of the Microscopy group, for offering a nice working environment. A special thanks to Mats Hättestrand, Tomas Liljenfors and Henrik Petterson for their friendship, humour and many interesting discussions. Also thanks to the ski / snow-board enthusiasts within the group for many memorable trips to Norway, the north of Sweden and France.

Dr. Anders Kvist for keeping the instruments in action and to Ola for helping when the computer was acting up even though it was a PC.

The staff of ESAB AB, who worked behind the scenes on this project. Special thanks to the present and past members of the Metallographic laboratory who always offered me great welcome while working there. Pål, Eva Lena and Håkan for help with instrumentation and for fruitful discussions, Daniela for much valued advice on specimen preparation.

ESAB AB is thanked for the production of experimental weld metals, permission to publish results and financial support. KK-stiftelsen of Sweden through the graduate school MARCHAL is thanked for additional financial support.

My many friends who give me so much joy in life. A special mention to you guys who have been there for me at one time or another... in Sweden, Maria, Paul and Sonja... in Ireland, Aidan, Caroline, Claire, Eric and Teresa... and in the USA, Jun Eu and Ulrike.

My many uncles, aunts and cousins who offer me great welcome, hospitality and kindness whenever I visit Ireland, England or the U.S.A.

My wonderful girlfriend Ann Charlott, for your friendship, love and for always being there for me.

Brian and Deirdre, for letting me know my place as a big brother... it is a tough job! My heartfelt thanks for caring about and supporting me!

Finally and most importantly, to my parents, for all that I am. Without you, I would not have lived some of my dreams, you are simply the best!!

Go raibh mile maith agaibh,

Enda Keenan

8. References

1. R.W.K. Honeycombe & H.K.D.K. Bhadeshia, Steel Microstructure and Properties, 2nd Ed., Edward Arnold, London, 1995.
2. L.-E. Svensson, Consumables for welding high strength steels. Svetsaren, 1999. 54 (1). (1)
3. D.J. Widgery, L. Karlsson, M. Muruganath & E. Keehan, Approaches to the development of high strength weld metals, 2nd Int. Symposium on High Strength Steel, Norway 2002. (37)
4. L.-E. Svensson: Control of microstructure and properties in steel arc welds, CRC Press, Inc., 1994
5. K. Easterling, Introduction to the Physical Metallurgy of Welding, Butterworths & Co Ltd., 1983.
6. C. Wildash, R.C. Cochrane, R. Gee, D. J. Widgery, Microstructural Factors Affecting Hydrogen Induced Cold Cracking in High Strength Steel Weld Metals, Trends in Welding Research, Georgia, USA, 1998.
7. P. Houldcrould and R. John, Welding and Cutting, Woodhead - Faulkner, Cambridge, U.K., 1998.
8. H. Ornig, H. Schutz, and P. Klug, Comparison of methods to determine the pre heat temperature for high - strength weld metals. Welding in the World, 41: p. 144 - 148, 1998.
9. J.F. Lancaster, Metallurgy of welding, 6th. Ed., Abington Publishing, 1999.
10. J. Lancaster, Handbook of structural welding, Abington Publishing, 1992.
11. Norman Bailey, Weldability of Ferritic Steels, Abington Publishing, 1994.
12. G. M. Evans and N. Bailey, Metallurgy of basic weld metal, Abington Publishing, 1999.
13. Mike Lord, Interpass temperature and the welding of strong steels. Welding in the World, 41: p. 452 - 459, 1998.
14. SSAB Oxelösund, WeldCalc, Version 1.0.0, 98 - 99
15. T.M. Noren and C. Pfeifer, Applied steel welding and metallurgy, ESAB, Gothenburg, Sweden.
16. K. Easterling, Introduction to the Physical Metallurgy of Welding, Butterworths, 1983.
17. J.C. F. Jorge, L.F. G. Souza, J.M. A. Rebello, G. M. Evans: Effect of Chromium on the mechanical properties of Mn - Mo weld metal deposits. II - A - 052 -99
18. H.K.D.H Bhadeshia, Bainite in Steels, The institute of materials, London, 1992
19. D. J. Widgery, Deoxidation practice and the toughness of mild steel weld metal, Ph. D. thesis, University of Cambridge, 1974
20. H.K.D.H. Bhadeshia, L.-E. Svensson, B. Grefoft, J. Mater. Sci., 21, 3947, 1986.
21. M. Lord, Design and modelling of ultra - High Strength Steel Weld Depos

- its, Ph. D. Thesis, Materials Science and Metallurgy, University of Cambridge, U.K., 1999.
22. T. Edvardson, H. Fredriksson & I. Svensson, *Met. Sci.* 10, 298, 1976.
 23. Z.Zhang, R.A. Farrar, Columnar grain development in C-Mn-Ni low-alloy weld metals and the influence of nickel, *J. Material. Science.*, 30: pp.5581-5588, 1995
 24. E.S. Davenport and E.C. Bain, *Trans. Met. Soc. A.I.M.E.* 90, 117, 1930.
 25. Electron microstructure of Bainite in Steels, 2nd Progress Report by Subcommittee XI of Committee E-4, *ASTM Proc.* 52, 543, 1952.
 26. Z. Nashiyama, *Sci. Rep. Tohoku Univ.*, 23, 325, 1934.
 27. G.V. Kurdjumov and G. Sachs, *Z. Phys.*, 64 325, 1930.
 28. G.V. Smith and R.F. Mehl, *Trans. AIME*, 150, 211-226, 1942.
 29. H.K.D.H. Bhadeshia and J.W. Christian, *Proc. of the Int. Conf. on Bainite*, ASMI, Chicago, USA, 1998.
 30. J. W. Christian, *The Strength of Martensite*, Chapter 5, Strengthening methods in crystals, A. Kelly and R. B. Nicholson, (Edits), Applied Science Publishers Ltd., London, 1971.
 31. P. G. Winchell and M. Cohen, *Trans., ASM*, 55, 347, 1962.
 32. H.K.D.H. Bhadeshia, Some phase transformations in steel. *Material Science and Technology*, 1999. 15: p. 22 - 29.
 33. W.C. Leslie, *Met. Trans.*, 3.5 (1972)
 34. ASM International, *Weld Integrity and Performance*, S. Lampman Tech. Ed., 1997.
 35. M. Hansen, *Constitution of Alloys*, McGraw-Hill Company Inc., New York, 1958
 36. J.C. F. Jorge, L.F. G. Souza, J.M. A. Rebello, G. M. Evans: Effect of Chromium on the mechanical properties of Mn - Mo weld metal deposits. II - A - 052 -99
 37. *Smithells Metals Reference Book*, 8th Edit., W.F. Gale & T.C. Totemier (Edits), (2004) Elsevier
 38. H.K.D.H. Bhadeshia, *Neural Networks in Materials Science*, ISIJ International (Japan), 39, p. 966 October, 1999.
 39. D.J.C. Mackay: *Neural Computation*. (1992), p. 448.
 40. D.J.C. Mackay: *Neural Computation*. (1992), p. 415.
 41. D.J.C. Mackay, "Mathematical modelling of weld phenomena 3", (ed. H. Cerjak), 359-389; *The Institute of Materials*, London, 1997.
 42. B. Sundman, B. Jansson and J. O. Andersson, The thermo-Calc databank system, *Calphad*, vol. 9, pp. 153-190, 1985
 43. B. Sundman, B. Jansson and J. O. Andersson, *Thermo-Calc, a Databank for calculation of phase equilibria and phase diagrams*, Division of physical metallurgy, KTH, Stockholm, Sweden, 1984

44. B. Sundman, Thermo-Calc, Version M, Users' guide, KTH, Stockholm, Sweden, April 1999.
45. G.-J. Cai, Microstructural and mechanical properties of high chromium steel weld metals, Ph. D. Thesis, Chalmers University of Technology, Gothenburg, Sweden, 1994.
46. W. D. Callister Jr., Materials Science and Engineering an Introduction, 4th Ed. J. Wiley, 1997.
47. Joesph Goldstein, Dale Newbury, David Joy, Charles Lyman, Patrik Echlin, Eric Lifshin, Linda Sawyer, Joesph Michael, Scanning Electron Microscopy and X-Ray Microanalysis, 3rd. Edit., Plenum Publishers, New York, 2003.
48. Leo Electronmikroskopie GmbH - LEO SUPRA 10.02 instrument information booklet.
49. L. Reimer, Image Formation in Low - Voltage Scanning Electron Microscopy, Vol. TT 12, SPIE Press, Washington, 1993.
50. R. Johnson, Environmental Scanning Electron Microscopy - An introduction to ESEM, Robert Johnson Associates, El Dorado Hills, CA, 1996.
51. B. G. Yacobi, D. B. Holt and L. L. Kazmerski, Microanalysis of Solids, Plenum Press, New York, 1994.
52. A.R. Lodding and U.S. Södervall, Chapter 1, Characterisation Compendium, Dept. of Physics, Chalmers University of Technology, Göteborg, Sweden, 2000.
53. H. Norden and A. Thölen, Electron Microscopy and Microanalysis Compendium, Dept. of Physics, Chalmers University of Technology, Göteborg, Sweden, 1997.
54. R. E. Smallman, Modern Physical Metallurgy, Butterworths, London, 1985
55. D. B. Williams and C. B. Carter, Transmission Electron Microscopy, Plenum Press, New York, 1996.
56. J. W. Edington, Practical Electron Microscopy in Material Science, The Macmillan Press Ltd., London (1975)
57. L. Reimer, Transmission Electron Microscopy, Springer Verlag, Berlin, 1993.
58. M. K. Miller, A. Cerezo, M. G. Hetherington, G. D. W. Smith, Atom Probe Field Ion Microscopy, Clarendon Press, Oxford, 1996, p. 483.
59. H. O. André, H. Norden, Scand. J. Metall. 8 (1979) 147.
60. H. O. André, J. Phys. 47 (C7) (1986) 483.
61. U. Rolander, H. O. André, J. Phys. 50 (C8) (1989) 529.
62. T. Kovacs, Principles of X - ray Metallurgy, ILIFFE Books Ltd., U.K., 1969.
63. Goldschmidt, Metallurgia, Vol. 40, page 103, 1949.
64. xrdcalc, <http://www.msm.cam.ac.uk/map/map.html>
65. M. Halvarsson, The microstructure and stability of CVD alumina coating, Ph. D. Thesis, Dept. of Physics, Chalmers University of Technology, Sweden, 1994.
66. <http://www.anter.com/TN69.htm>

67. M. Hättestrand, Precipitation Reactions at High Temperatures on 9 - 12 % Chromium Steels, Ph. D. Thesis, Dept. of Physics, Chalmers University of Technology, Sweden, 2000.
68. W. Rong, Fine scale microstructure of high speed steels, Ph. D. thesis, Dept. of Physics, Chalmers University of Technology, Sweden, 1985

Appendix: The Papers

Paper I

M. Muruganath, H.K.D.H. Bhadeshia, E. Keehan, H.-O. Andrén, L. Karlsson: Strong and Tough Steel Welds, Proc. 6th Inter. Seminar, “Numerical Analysis of Weldability”, Graz, Austria, Oct. 1-3, 2001.

Paper II

E. Keehan, H. O. Andrén, L. Karlsson, M. Muruganath, H. K. D. H. Bhadeshia, Microstructural and mechanical effects of nickel and manganese on high strength steel weld metals, 6th Int. Conference on Trends in Welding Research, Pine Mountain, Georgia, USA, April 15-19, 2002.

Paper III

E. Keehan, H. K. D. H. Bhadeshia, H.-O. Andrén, L. Karlsson, L.-E. Svensson, Microstructure characterisation of a high strength steel weld metal containing the novel constituent coalesced bainite, In manuscript

Paper IV

E. Keehan, L. Karlsson, H.-O. Andrén, Influence of C, Mn and Ni contents on microstructure and properties of strong steel weld metals — Part I. Effect of nickel content, In manuscript

Paper V

E. Keehan, L. Karlsson, H.-O. Andrén, H. K. D. H. Bhadeshia, Influence of C, Mn and Ni contents on microstructure and properties of strong steel weld metals — Part II. Impact toughness gain from manganese reductions, In manuscript

Paper VI

E. Keehan, L. Karlsson, H.-O. Andrén, H. K. D. H. Bhadeshia, Influence of C, Mn and Ni contents on microstructure and properties of strong steel weld metals — Part III. Increased strength from carbon additions, In manuscript

Paper VII

E. Keehan, M. Muruganath, L. Karlsson, H.-O. Andrén, H. K. D. H. Bhadeshia, New developments with C-Mn-Ni high strength steel weld metals — Part A. Microstructure, In Manuscript

Paper VIII

E. Keehan, L. Karlsson, H.-O. Andrén, L.-E. Svensson, New developments with C-Mn-Ni high strength steel weld metals — Part B. Mechanical Properties, In Manuscript

Paper IX

L. Karlsson, E. Keehan, H.-O. Andrén, and H. K. D. H. Bhadeshia, Development of High Strength Steel Weld Metals – Potential of novel high-Ni compositions, Eurojoin 5, Vienna, 13-14 May, 2004